Pollution trace gas distributions and their transport in the Asian monsoon upper troposphere and lowermost stratosphere during the StratoClim campaign 2017

Sören Johansson[1], Michael Höpfner[1], Oliver Kirner[2], Ingo Wohltmann[3], Silvia Bucci[4], Bernard Legras[4], Felix Friedl-Vallon[1], Norbert Glatthor[1], Erik Kretschmer[1], Jörn Ungermann[5], and Gerald Wetzel[1]

[1]Institute of Meteorology and Climate Research, Karlsruhe Institute of Technology, Karlsruhe, Germany
[2]Steinbuch Centre for Computing, Karlsruhe Institute of Technology, Karlsruhe, Germany
[3]Alfred Wegener Institute, Helmholtz Center for Polar and Marine Research, Potsdam, Germany
[4]Laboratoire de Météorologie Dynamique, UMR8539, IPSL, CNRS/PSL-ENS/Sorbonne Université/École polytechnique, Paris, France
[5]Institute of Energy and Climate Research - Stratosphere (IEK-7), Forschungszentrum Jülich, Jülich, Germany

Correspondence: S. Johansson (soeren.johansson@kit.edu)

Abstract. We present the first high resolution measurements of pollutant trace gases in the Asian Summer Monsoon Upper Troposphere and Lowermost Stratosphere (UTLS) from the Gimballed Limb Observer for Radiance Imaging of the Atmosphere (GLORIA) during the StratoClim (Stratospheric and upper tropospheric processes for better climate predictions) campaign with base in Kathamandu, Nepal, 2017. Measurements of peroxyacetyl nitrate (PAN), acetylene (C_2H_2), and formic acid (HCOOH)

5   show strong local enhancements up to altitudes of 16 km. More than 500 pptv of PAN, more than 200 pptv of C_2H_2, and more than 200 pptv of HCOOH are observed. An observed local maximum of PAN and C_2H_2 at altitudes up to 18 km, reaching to the lowermost stratosphere, instead has been transported for a longer time. A local minimum of HCOOH is correlated with a maximum of ammonia (NH_3), which suggests different wash out efficiencies of these species in the same air masses. To study the influence of convective transport to the measured pollution trace gas occurrences in detail, a trajectory analysis of the

10   models ATLAS and TRACZILLA examined backward trajectories, starting at geolocations of GLORIA measurements with enhanced pollution trace gases. Both trajectory schemes implemented advanced techniques for detection of convective events. These convective events along trajectories leading to GLORIA measurements with enhanced pollutants are located close to regions, where satellite measurements by OMI show enhanced tropospheric columns of nitrogen dioxide (NO_2) in the days prior to the observation. As an application of these highly resolved measurements, a comparison to the atmospheric models

15   CAMS and EMAC is performed. It is demonstrated that these simulation results are able to reproduce large scale structures of the pollution trace gas distributions if the convective influence on the measured air masses is captured by the meteorological fields used by these simulations. Both models do not have sufficient horizontal resolution to capture all the convective events that are necessary to reproduce the fine structures measured by GLORIA. To investigate the influence of the strength of non-methane volatile organic compounds (NMVOCs) emissions in the EMAC model, sensitivity studies with artificially enhanced

20   NMVOC emissions are performed. With these enhanced emissions, the simulation results succeed to reproduce the measured peak values of the pollutants, but do not improve the comparison of spatial distributions.

1 Introduction

During the Asian Summer Monsoon (ASM), a large-scale persistent anticyclonic circulation, the so-called Asian Monsoon Anticyclone (AMA), exists in the upper troposphere. Convective processes are able to inject polluted lower tropospheric air masses into the AMA (Randel and Jensen, 2013; Vogel et al., 2015; Pan et al., 2016; Basha et al., 2019; Legras and Bucci, 2019).

5 So far, most observational information of the Upper Troposphere and Lowermost Stratosphere (UTLS) composition during the ASM has been obtained by satellite limb-sounding experiments (e.g., Santee, 2017) which are, however, restricted by low vertical and horizontal resolution and sampling. Airborne in-situ observations of airmasses inside the AMA are extremely sparse and often sample only filaments or the border areas of the AMA. Here we present data from the first dedicated aircraft campaign sampling air from the central region of the AMA.

10 In the contemporary understanding, the chemical composition of the confined system of the AMA is dominated by enhanced amounts of tropospheric trace gases, such as water vapor (H_2O) and carbon monoxide (CO), which are transported to higher altitudes (Santee, 2017). It has been shown that pollutants, such as ammonia (NH_3) or peroxyacetyl nitrate (PAN) are first transported to the upper troposphere and then confined there until the breakup in late summer (Höpfner et al., 2016; Ungermann et al., 2016). These pollutants play an important role in the formation of upper tropospheric ozone and aerosol (Singh, 1987;

15 Höpfner et al., 2019). Airborne in-situ measurements of filaments with polluted monsoon air masses have revealed that O_3 increases in the AMA outflow in tropospheric air (Gottschaldt et al., 2018). Based on in-situ measurements of another aircraft campaign, Lelieveld et al. (2018) formulated the picture of the AMA as a pollution pump and purifier by OH of the polluted air masses, originating from South Asian emissions: Due to the production of OH by reactions with lightning NO_x in the upper troposphere, the polluted air masses are processed with the available OH. Several model studies identified the impact

20 of different source regions and long-range transport to the AMA, either with artificial tracers (e.g., Vogel et al., 2015, 2016, 2019) or e.g., CO as a proxy (Pan et al., 2016; Cussac et al., 2020). Large discrepancies are observed in radiative heating rates and upward transport between different reanalyses (Randel and Jensen, 2013). However, observational data of the chemical composition of the upper troposphere inside the ASM are sparse.

The first observations of the upper tropospheric chemical composition in high vertical resolution have been obtained during

25 the StratoClim (Stratospheric and upper tropospheric processes for better climate predictions) campaign. This study presents and discusses a unique data set of pollution trace gases measured during this campaign, in particular non-methane volatile organic compounds (NMVOCs), in the Asian monsoon UTLS. StratoClim has been the first high-altitude airborne campaign with observations in the UTLS inside the AMA. These data were obtained with the Gimballed Limb Observer for Radiance Imaging of the Atmosphere (GLORIA) during this StratoClim aircraft campaign 2017, with base in Kathmandu, Nepal. One

30 goal of the GLORIA measurements was to identify and quantify the spatial distribution of the pollution trace gases PAN, C_2H_2, and HCOOH, together with HNO_3 and O_3 in the Asian monsoon UTLS. In addition, atmospheric chemistry models that simulate the Asian monsoon are sparsely evaluated due to the low number of detailed observations in the UTLS.

In this study, we apply this unique set of NMVOC measurements in the UTLS during the Asian monsoon in two directions. First, the origin of polluted air masses is investigated through two trajectory models allowing advanced schemes for detection

of convective vertical transport times and areas. Second, a first evaluation of two atmospheric chemistry models is provided and suggests improvements for these models based on the comparisons with the GLORIA measurements.

In the following section, methods and data sets are introduced: The discussed pollution trace gases are briefly characterized, the StratoClim aircraft campaign is described and the GLORIA measurements and data evaluation explained, and the atmospheric models applied here are introduced. Then, the GLORIA measurements are discussed (section 3), followed by the analysis of ATLAS and TRACZILLA backward trajectories from regions of interest identified by the GLORIA measurements (section 4). The following section (section 5) presents a comparison to the atmospheric chemistry models EMAC and CAMS. The last section before the conclusion (section 6) discusses the influence of increased NMVOC emissions in the EMAC model.

2 Data sets and methods

2.1 Measured trace gases

The scientific analysis of the trace gas measurements will be based on five species, which are briefly introduced in the following paragraphs. Focus is put on sources and sinks of these species, their lifetimes in the atmosphere, and reports of earlier measurements.

2.1.1 Nitric acid

Nitric acid (HNO_3) is a trace gas with maximum mixing ratios of several ppbv in the stratosphere (e.g., Brasseur and Solomon, 2005). In the troposphere, HNO_3 typically has mixing ratios less than 1 ppbv. Atmospheric HNO_3 acts as a sink of tropospheric nitrogen oxide (NO_x, e.g.: $NO_2 + OH \rightarrow HNO_3$) but is also part of a variety of other chemical reactions, which are not mentioned here in detail (see e.g., Burkholder et al., 2015).

There is a large number of spaceborne HNO_3 observations reaching down into the upper troposphere, e.g., volume mixing ratio (VMR) profiles from the Microwave Limb Sounder (MLS; Santee et al., 1998, 2007), the Atmospheric Chemistry Experiments - Fourier Transform Spectrometer (ACE-FTS; Wolff et al., 2008) or the Michelson Interferometer for Passive Atmospheric Sounding on the Envisat satellite (von Clarmann et al., 2009, MIPAS). Airborne measurements have been performed in-situ using chemical ionization mass spectrometer techniques (e.g., Neuman et al., 2001; Jurkat et al., 2016), and also with remote sensing techniques (e.g., Braun et al., 2019). In the ASM, HNO_3 is used as stratospheric tracer to demonstrate the isolation of the AMA (Park et al., 2008) and within the transport and chemistry of PAN (Fadnavis et al., 2014). In this paper, HNO_3 measurements serve as complementary information and are not analyzed in detail.

2.1.2 Ozone

Ozone (O_3), similar to HNO_3, has its maximum in the stratosphere, but with much higher mixing ratios of several ppmv (e.g., Brasseur and Solomon, 2005). Due to the importance of the stratospheric ozone layer, stratospheric O_3 is continuously monitored (WMO, 2019). Tropospheric enhancements of O_3 typically can reach up to several hundred ppbv. Sources of tro-

pospheric O_3 are stratosphere-troposphere exchange processes, and catalytic reactions with nitrogen oxides (Brasseur and Solomon, 2005). Thus, tropospheric O_3 can be an indicator of polluted air masses. Loss of tropospheric O_3 is caused by photolysis, and reactions with OH. For that reason, moist and clean air masses are correlated with rather low O_3 mixing ratios. During the Asian monsoon, typically low tropospheric O_3 mixing ratios are measured due to uplift of moist and clean air from

5   the Indian ocean (Safieddine et al., 2016).

Measurements of O_3 in the upper troposphere are available e.g., VMR profiles from MLS (Froidevaux et al., 1994; Livesey et al., 2008), ACE-FTS (Sheese et al., 2016), MIPAS (von Clarmann et al., 2009), from airborne in-situ (e.g., Browell et al., 1987; Zahn et al., 2012; Safieddine et al., 2016) and airborne remote sensing measurements (e.g., Browell et al., 1987; Woiwode et al., 2012). During recent Asian monsoon seasons, balloon-borne ozone sondes have been launched (e.g., Bian

10 et al., 2012; Brunamonti et al., 2018; Li et al., 2018). Similarly to HNO_3, measurements of O_3 in the ASM is used as an indicator of stratospheric air masses and of polluted air (Park et al., 2007, 2008).

2.1.3 Peroxyacetyl nitrate

Peroxyacetyl nitrate (PAN) is a secondary pollutant formed by the reaction of peroxyacetyl with nitrogen dioxide:

$$CH_3COO_2 + NO_2 + M \rightarrow CH_3COO_2NO_2 + M \tag{R1}$$
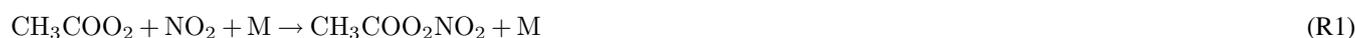
15 Peroxyacetyl is a product of oxidation or photolysis of NMVOC, which are emitted from fuel combustion and biomass burning (Fischer et al., 2014). PAN is mainly destroyed by thermal decomposition to the starting species of reaction (R1), whereas dry deposition and photolysis play a minor role. While the lifetime of PAN is very short at lower altitudes (1 h at 298 K), it becomes progressively longer and reaches around 5 months at higher altitudes (250 K). This makes PAN useful as a tracer for upper tropospheric transport studies (Singh, 1987; Glatthor et al., 2007; Fischer et al., 2014).

20 PAN VMR observations are reported from the spaceborne instruments ACE-FTS (Coheur et al., 2007), MIPAS-Envisat (Glatthor et al., 2007; Wiegele et al., 2012), CRISTA (Ungermann et al., 2016), and column information from IASI (Infrared Atmospheric Sounding Interferometer; Coheur et al., 2009). Airborne measurements were achieved from instruments with remote sensing (CRISTA-NF; Ungermann et al., 2013), and in-situ (e.g., Singh et al., 2001) measurement techniques. In the ASM, measurements of PAN have been applied to study transport and impact of polluted air masses (Fadnavis et al., 2014).

25 Typically, PAN is strongly enhanced within the main part of the AMA (Ungermann et al., 2016).

2.1.4 Acetylene

Acetylene or ethyne (C_2H_2) is a tropospheric substance with mixing ratios of few pptv in maximum and a product of combustion of bio- and fossil fuels and biomass burning. The reaction with OH is the major sink of C_2H_2 in the troposphere. Compared to PAN, C_2H_2 has a rather short lifetime of 2 weeks (Xiao et al., 2007). Measurements of C_2H_2 VMR profiles have

30 been reported by e.g., ATMOS (Rinsland et al., 1987), ACE-FTS (Rinsland et al., 2005), and MIPAS-Envisat (Wiegele et al., 2012). Within the ASM, measurements of C_2H_2 have been used as tropospheric tracer to study the chemical isolation of the AMA (Park et al., 2008) .
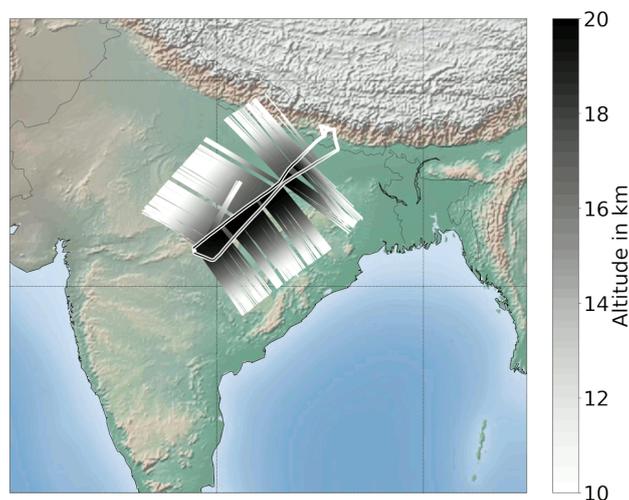
Figure 1. Flight path and tangent altitudes of StratoClim research flight on 31 July 2017. The bold line indicates the flight path and aircraft altitude of Geophysica, while small across-track lines indicate the position and altitude of tangent altitudes of GLORIA measurements. The map is centered at the Indian subcontinent.

2.1.5 Formic acid

Formic acid (HCOOH) mainly exists in the troposphere (with mixing ratios smaller than 1 ppbv) and originates from biogenic emissions, biomass burning and fossil fuel combustion (Mungall et al., 2018). In contrast to PAN and C_2H_2, HCOOH is water soluble, such that its major tropospheric sink is wet deposition (depending on acidity). Further sinks are reaction with OH, and dry deposition (Paulot et al., 2011). The average atmospheric lifetime is estimated to 2-4 days, while the lifetime is shorter in the boundary layer and longer in the free troposphere (Millet et al., 2015). Measurements of atmospheric HCOOH VMR profiles are available e.g., from ACE-FTS (Rinsland et al., 2006), MIPAS-Envisat (Grutter et al., 2010) and column information from IASI (Coheur et al., 2009). Airborne measurements in the UTLS are reported by e.g., Reiner et al. (1999) or Singh et al. (2000). To our knowledge, no studies using measurements HCOOH in the ASM upper troposphere have been published so far.

2.2 StratoClim aircraft campaign and GLORIA observations

During the Asian summer monsoon 2017, the StratoClim aircraft campaign was performed with basis in Kathmandu, Nepal. In total, 22 in-situ and 3 remote sensing instruments were integrated into the Russian high altitude research aircraft M55 Geophysica. As part of the remote sensing payload, GLORIA was deployed during four research flights of this measurement campaign. In this work, we will discuss the research flight on 31 July 2017. The flight path of this deployment is shown in Fig. 1.

GLORIA is a unique airborne imaging limb infrared sounding instrument (Friedl-Vallon et al., 2014; Riese et al., 2014), which has been operated during several campaigns with the German HALO research aircraft and with M55 Geophysica. The

Table 1. Retrieval properties for HNO_3, O_3, PAN, C_2H_2 and HCOOH: Used spectral regions and handling of interfering species. 10 and 90 percentile ranges are given for vertical resolution and estimated errors. In the supplement it is shown that larger absolute errors are typically connected to higher VMRs.

Target gas	spectral regions in cm^{-1}	fitted species	forward-calculated species	vertical resolution	estimated error
HNO_3	867.0000 - 870.0000	HNO_3, NH_3, OCS	$H_2O^{\dagger}$	0.7 - 0.9 km	70 - 220 pptv
O_3	780.6250 - 781.7500 985.0000 - 988.0000	O_3	H_2O, CO_2	0.5 - 1.3 km	70 - 200 ppbv
PAN	780.3125 - 790.0000 794.0000 - 805.0000	PAN, H_2O, O_3, CCl_4	CO_2, $HNO_3^{\dagger}$, CFC-22, CFC-113, $ClONO_2$, HNO_4	0.5 - 0.8 km	50 - 120 pptv
C_2H_2	759.5625 - 759.8125 766.5625 - 766.8125 775.9375 - 776.3125 780.5000 - 780.8750	C_2H_2, O_3	$H_2O^{\dagger}$, CO_2, NO_2, $NH_3^{\dagger}$, $HNO_3^{\dagger}$, HCN, CH_3Cl, $C_2H_6^{\dagger}$, COF_2, CFC-22, CCl_4, N_2O_5, $ClONO_2$, CH_3CCl_3, $PAN^{\dagger}$	0.7 - 1.0 km	30 - 60 pptv
HCOOH	1103.5000 - 1106.1250 1112.5000 - 1116.8750	HCOOH	$H_2O^{\dagger}$, $O_3^{\dagger}$, CH_4 CFC-11, CFC-12, CFC-113	0.7 - 1.0 km	30 - 70 pptv

† Results of previous retrievals (not necessarily shown in this paper) targeting these species have been used for simulation of the spectra.

main part of GLORIA is a Michelson Fourier Transform Spectrometer combined with an imaging detector, which allows for simultaneous measurements of 127×48 spectra. Further, GLORIA consists of two external black bodies for in-flight radiometric calibration and a gimbal frame for active corrections of aircraft movements and line of sight control. Interferograms used in this study are from the "high spectral resolution" mode with 8.0 cm optical path difference, which results in spectra
5   with 0.0625 cm^{-1} sampling.

These measured spectra are then used to retrieve profiles of atmospheric trace gases and particles. The retrieval is performed using a nonlinear least-squares fit with Tikhonov regularization. The overall retrieval strategy is explained in detail by Johansson et al. (2018). Main differences compared to this retrieval strategy are the applied cloud filter and the handling of continua in the radiative transfer model KOPRA (Stiller, 2000): Due to the high mixing ratios of aerosols (Höpfner et al., 2019), cloud
10   filtering using the MIPAS "cloud index" method (Spang et al., 2004) was replaced by filtering according to mean radiance between 850 cm^{-1} and 970 cm^{-1} with a threshold of 800 nW $(cm^2 \ sr \ cm^{-1})^{-1}$. Due to highly structured distributions of aerosol and thin cirrus, the retrieval of a spectrally flat extinction was substituted by retrieving a multiplicative scale and an additive radiance offset parameter for each vertical point in the retrieval altitude grid. For the HNO_3 retrieval, a pre-fitted scale from the spectral region 955.8750 - 958.4375 cm^{-1} has been used and only the offset was fitted (instead of scale and offset).
15   Spectral ranges for the retrievals for each discussed trace gas and the handling of interfering species are summarized in Tab. 1, together with typical vertical resolutions and estimated errors. Detailed plots of estimated errors and vertical resolutions are provided as supplement of this paper.

2.3 Atmospheric model simulations

2.3.1 EMAC

The ECHAM/MESSy Atmospheric Chemistry (EMAC) model is a numerical chemistry and climate simulation system that includes sub-models describing tropospheric and middle atmosphere processes and their interaction with oceans, land and
5 human influences (Jöckel et al., 2010). It uses the second version of the Modular Earth Submodel System (MESSy2) to link multi-institutional computer codes. The core atmospheric model is the 5th generation European Centre Hamburg general circulation model (ECHAM5, version 5.3.02 Roeckner et al., 2006). For the present study we applied EMAC (ECHAM5 version 5.3.02, MESSy version 2.53) in the T106L90MA-resolution, i.e. with a spherical truncation of T106 (corresponding to a quadratic Gaussian grid of approx. 1.125 by 1.125 degrees in latitude and longitude) with 90 vertical hybrid pressure
10 levels up to 0.01 hPa (approx. 80 km). The chemistry setup in the chemistry submodel MECCA (Sander et al., 2011) was expanded (in contrast to the standard chemistry) with regard to a better simulation of PAN and the tropospheric chemistry. It compromises 460 chemical substances, 1187 gas phase reactions, and 262 photolyses. We performed a standard simulation and two sensitivity simulations with additional 50% and additional 100% emissions of NMVOC. In all three simulations the meteorological fields were specified by ECMWF ERA-Interim (Dee et al., 2011) and all simulations were initialized on 1 May
15 2017.

2.3.2 CAMS

The Copernicus Atmosphere Monitoring Service (CAMS) reanalysis (CAMSRA) from the European Centre for Medium-Range Weather Forecasts (ECMWF) is an atmospheric composition model, focusing on the troposphere. CAMS applies the ECMWF IFS (Integrated Forecast System) model and assimilates various satellite measurements of atmospheric composition.
20 It uses the chemistry module IFS(CB05) (Flemming et al., 2015) and the aerosol module as decribed in Morcrette et al. (2009). Apart from assimilated ozone, CAMS does not simulate stratospheric chemistry. The model uses 60 vertical hybrid pressure levels, with the top level at 0.1 hPa and has a horizontal resolution of 80 km. Output is provided every 3 hours. The data set is characterized in detail by Inness et al. (2019). In a model evaluation study by Wang et al. (2019), trace gas measurements from aircraft campaigns were compared to CAMS reanalysis data.

25 2.3.3 TRACZILLA

The TRACZILLA model (Pisso and Legras, 2008) is a modified version of the Lagrangian model FLEXPART (Stohl et al., 2005; Legras et al., 2005). Trajectories are launched at GLORIA tangent points at the rate of 1000 per point. They are integrated backward in time for one month, using the ECMWF reanalysis horizontal winds (ERA-5, 1 h temporal resolution), and diabatic vertical motions. The TRACZILLA simulations are run on a $0.25° \times 0.25°$ (latitude $\times$ longitude) grid at 137 vertical levels in
30 the spatial domain 10°W to 160°E, and 0°N to 50°N.

A diffusion with a diffusion coefficient of $D=0.1$ m^{2}s^{-1} is added (based on previous studies in the subtropics, Pisso and Legras, 2008; James et al., 2008), represented by a random walk equivalent, that disperses the cloud of parcels from each point. A convective source is then individuated when a trajectory is found with a pressure higher than the pressure of a convective cloud top, as similarly done in Tissier and Legras (2016). We use here the cloud top products provided by the SAF-NWC (EUMETSAT Satellite Application Facility for Nowcasting) software package (Derrien et al., 2010; Sèze et al., 2015) from MSG1 (Meteosat 8) and Himawari geostationary satellites. More details on the algorithm and its evaluation against trace gas measurements can be found in Bucci et al. (2020) and Legras and Bucci (2019).

2.3.4 ATLAS

Trajectories from the ATLAS model (Wohltmann and Rex, 2009) are driven by the European Centre for Medium-Range Weather Forecasts European Reanalysis 5 (ERA5) ($1.125° \times 1.125°$ horizontal resolution, 137 vertical levels, 3 h temporal resolution). The model uses a hybrid coordinate transforming from pressure at the surface to potential temperature at the tropopause (Wohltmann and Rex, 2009). In the altitude range of GLORIA, the coordinate is a potential temperature coordinate in good approximation, and the trajectories can be regarded as diabatic trajectories driven by the total heating rates of ERA5. Time step is 10 minutes.

The trajectory model includes a detailed stochastic parameterization of convective transport driven by ERA5 convective mass fluxes and detrainment rates (Wohltmann et al., 2019). In addition, a vertical diffusion of $D=0.1$ m^{2}s^{-1} is added to every trajectory, consistently with TRACZILLA. At every measurement location of GLORIA, 1000 backward ensemble trajectories are started, which take different paths due to the stochastic nature of the convective transport scheme. A convective event is detected by drawing a uniformly distributed random number between 0 and 1 every 10 minutes and comparing that to the calculated probability for detrainment from ERA5 at the location of the trajectory. If the random number is smaller than the calculated probability, it is assumed that a convective event was encountered.

In an analysis of the ATLAS trajectories, the influence of the usage of ERA5 or ERA-Interim as meteorological fields, the influence of applied vertical diffusion, and the influence of the usage of kinematic or diabatic trajectories was investigated (not shown). This analysis (and also similar analyses by Legras and Bucci (2019)) revealed that major differences for the ATLAS trajectories occur between the usage of ERA5 or ERA-Interim meteorological fields, while diffusion and kinematic/diabatic trajectories only have minor influences.

2.3.5 OMI NO$_2$ tropospheric column

The Ozone Monitoring Instrument (OMI) is a nadir looking ultraviolet-visible spectrometer instrument onboard the NASA Aura satellite. Targeted quantities are columns of trace gases (such as O$_3$, NO$_2$, SO$_2$), aerosol properties, cloud top heights and surface irradiances (Levelt et al., 2006). In this work, we use the troposheric column of nitrogen dioxide (NO$_2$) as a proxy for pollutant emissions (Crutzen, 1979). OMI NO$_2$ is provided as cloud-filtered daily level-3 product on a $0.25° \times 0.25°$ grid (Krotkov, 2013). For the analysis in Sec. 4, 14 days of OMI NO$_2$ measurements are averaged to indicate regions of pollutant emissions prior to the measurement.

3   Pollution trace gases measured during StratoClim flight on 2017-07-31

GLORIA measurements of pollution trace gases introduced in Sec. 2.1 are shown as horizontal distributions on a map, and as vertical distributions in Fig. 2, and regions that are discussed in this and following sections are marked with colored boxes. As expected, the HNO_3 VMRs (Fig. 2b) strongly increase above the tropopause at 17 km to typical stratospheric values of more than 2 ppbv. Around the tropopause at 17 km, fluctuations of HNO_3 up to 0.5 ppbv can be observed. In the first part of the flight (until 4:45 UTC), also structures of local enhancements up to 0.5 ppbv are visible below the tropopause at altitudes between 14 km and 16 km. In particular, enhancements are noted at 16 km at 4:00 UTC moving down to 15 km at 4:15-4:50 UTC (marked with a magenta box). In the second flight part, at 17 km altitude and 5:45 UTC, a local maximum of 0.5 ppbv HNO_3 is visible, together with a local minimum above, at 18 km altitude.

Measured O_3 (Fig. 2d) shows similar distributions as HNO_3: Above 19 km altitude, elevated VMRs of more than 1000 ppbv are measured in the same region where the HNO_3 measurements show stratospheric values. Above and around the 380 K tropopause, O_3 mixing ratios between 200 ppbv and 400 ppbv are measured. During the second part of the flight, around 5:30 UTC, a local maximum of O_3 up to 400 ppbv was observed between 15 km and 16.5 km (purple box), but these measurements have relatively high total estimated errors up to 180 ppbv, which is within the magnitude of this local enhancement (see Supplementary Fig. 4).

PAN vertical distributions (Fig. 2f) show how different the air masses sampled with GLORIA have been: The first part (until 4:45 UTC) indicates enhanced PAN mixing ratios of more than 500 pptv up to the flight altitude of 18 km. Maximum values are observed at 4:10 UTC at 16 km altitude (marked with a red box). A local minimum can be found in the same region of the HNO_3 local maximum (magenta box). These retrieved structures come with larger uncertainties compared to other parts of this flight, due to stronger spectral extinction observed at these altitudes in this part of the flight. The rather broadband spectral signature of PAN makes it more difficult for the retrieval to discriminate between the spectral offset due to aerosol or cirrus clouds, and the targeted spectral emission of PAN. The second part of the flight shows PAN background mixing ratios of 150 pptv in the troposphere and 100 pptv in the stratosphere. At lower altitudes, below 14 km, again enhanced mixing ratios of more than 500 pptv are observed between 5:00 and 5:30 UTC (orange box). Later during this flight, at 6:00 UTC, background values are observed at similar altitudes (blue box). Directly at and above the thermal tropopause, a local enhancement of 250 - 400 pptv of PAN is measured in this second part of the flight (cyan box).

As for PAN, vertical distributions of C_2H_2 (Fig. 2h) show a large vertical variability during the first part of the flight. A local maximum up to 200 pptv is observed at 4:10 UTC at 16 km altitude (marked with a red box) and as for PAN a local minimum is visible below (magenta box). Below 14 km altitude, VMRs between 100 pptv and 200 pptv are measured. The second part of the flight shows strong enhancements of C_2H_2 of more than 200 pptv at altitudes below 14 km between 5:00 and 5:30 UTC (orange box), where PAN showed enhancements, too. The same local minimum as for PAN is observed at similar altitudes but later during the flight (6:00 UTC, blue box). Above the tropopause (cyan box), a faint local maximum with VMRs up to 100 pptv appears in the measurements.
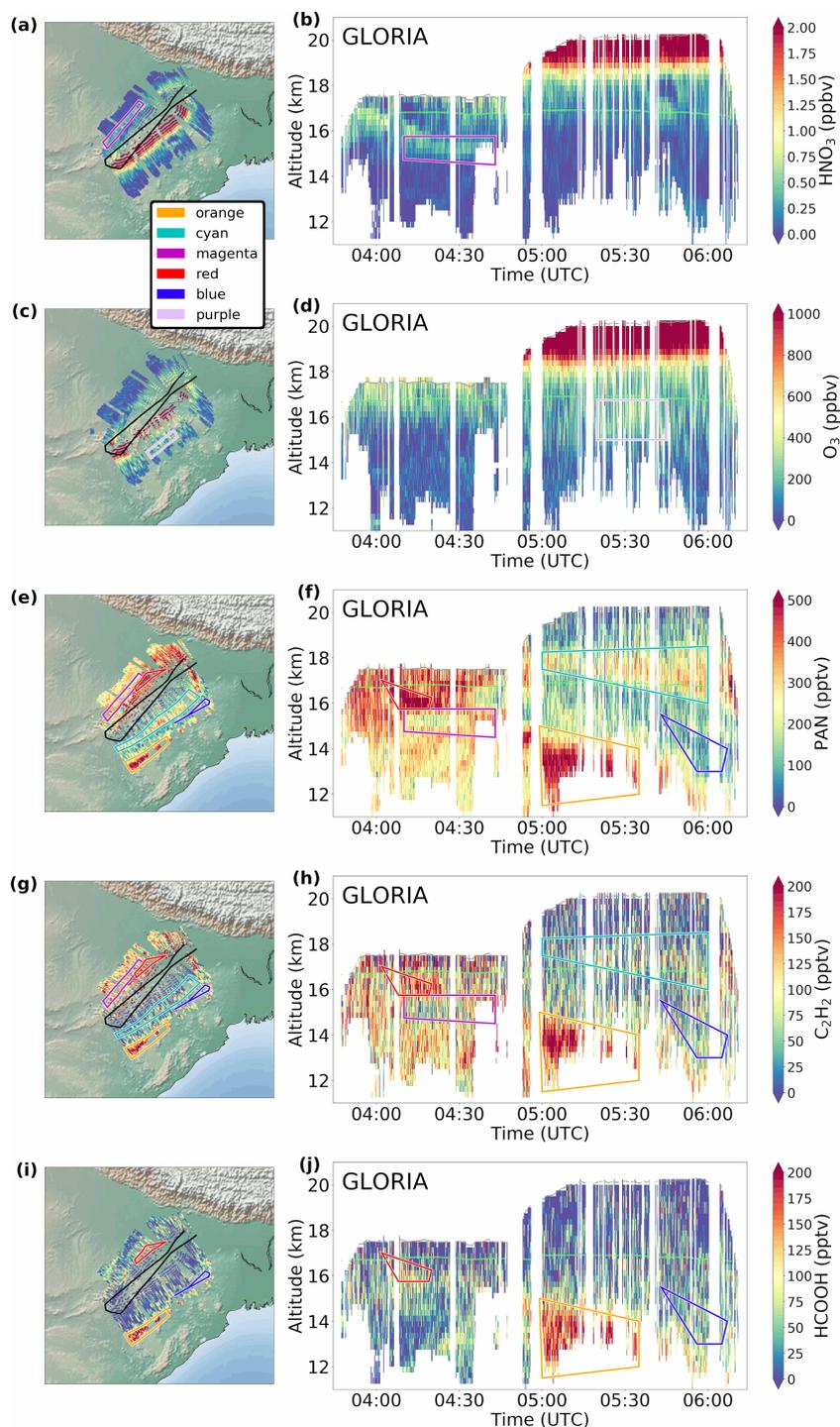
Figure 2. Horizontal (left column) and vertical (right column) distributions of GLORIA measurements of (a-b) HNO_3, (c-d) O_3, (e-f) PAN, (g-h) C_2H_2, (i-j) HCOOH for StratoClim flight on 31 July 2017. The black line in the maps shows the flight path, and the green line the 380 K potential temperature isentrope as approximate tropopause altitude. Colored boxes mark regions of interest, which are discussed in the following sections. The maps are centered at the Indian subcontinent.

Unlike PAN and C_2H_2, HCOOH does not have these enhanced VMRs at and above the tropopause of the second part of the flight. Enhancements of HCOOH are observed in the first part of the flight at 4:10 and 16 km altitude (red box) and at 4:20 and 13 km altitude. In the second part of the flight, as for all other gases than HNO_3, considerably large HCOOH of more than 200 pptv is observed below 14 km between 5:00 and 5:30 UTC (orange box) and a local minimum is measured at similar

5   altitudes at 6:00 UTC (blue box). In the beginning of the flight (until 04:15 UTC), below 15 km, a minimum of HCOOH is measured, while PAN and C_2H_2 are present. This is the same region, where Höpfner et al. (2019) reported strongly enhanced mixing ratios of NH_3. This HCOOH local minimum is present, despite enhancements of HCOOH total columns (measured by the Infrared Atmospheric Sounding Interferometer; IASI) at the border region between Pakistan and India (see Suppl. Fig. 11), the region identified as source for the enhanced NH_3. The trajectory analysis by Höpfner et al. (2019) indicated transport times

10   of 3 days since convection, which is within the atmospheric lifetime of HCOOH. This presence of PAN and C_2H_2 and the absence of HCOOH suggests that the loss of HCOOH was induced by wet deposition, which was more efficient for HCOOH than for NH_3. Both species, HCOOH and NH_3, are water soluble, but HCOOH has a considerably higher Henry coefficient compared to NH_3. In addition, the solubility is known to be also dependent on the pH of the liquid. (see e.g., Seinfeld and Pandis, 2016) While HCOOH is acidic, NH_3 is alkaline, which is a possible explanation for HCOOH being washed out

15   completely, while NH_3 is still present in large VMRs in the same air masses. As mentioned above, later during this flight, also strongly enhanced concentrations of HCOOH are observed. This indicates that air masses lifted by convection to high altitudes are not always depleted of HCOOH by washout processes.

The GLORIA measurements show how different the two parts of the flight have been regarding the composition of the measured air masses: In the first part of the flight, high VMRs of all discussed gases have been detected up to the tropopause

20   at 17 km, while during the second part of the flight, such high abundances have been only detected up to 14 km altitude. This difference between the flight legs is also discussed by Höpfner et al. (2019), who found large abundances of ammonia (NH_3) in the first part of the flight, but none in the second. On the map projections, it can be seen that the tangent points of the measurements point in opposite directions for the different flight parts: Lines of sight of the outbound flight leg point towards north-west and those of the inbound flight leg point towards south-east. In addition, trajectory calculations from Höpfner et al.

25   (2019) suggest that air masses observed during the first part of the flight were strongly influenced by convection a few days before the observations. The beginning of the second part of the flight shows below 15 km strong enhancements of pollution trace gases, which is also an indication of convective events (which is discussed later in this paper). The enhancements at and above the tropopause of the second flight part (cyan box) in PAN and C_2H_2, but not in HCOOH suggests that these air masses are older than a few days (lifetime of HCOOH), but younger than 2 weeks (lifetime of C_2H_2). A detailed analysis of the origin

30   of measured regions of interest (marked by colored boxes) is discussed in Sec. 4.

4   Trajectory analysis: Origin of polluted air masses

To gain more insight about the origin of polluted air through convective processes, here we apply backward trajectories from the models TRACZILLA and ATLAS to estimate the origin of measured polluted air masses. Due to the high influence of
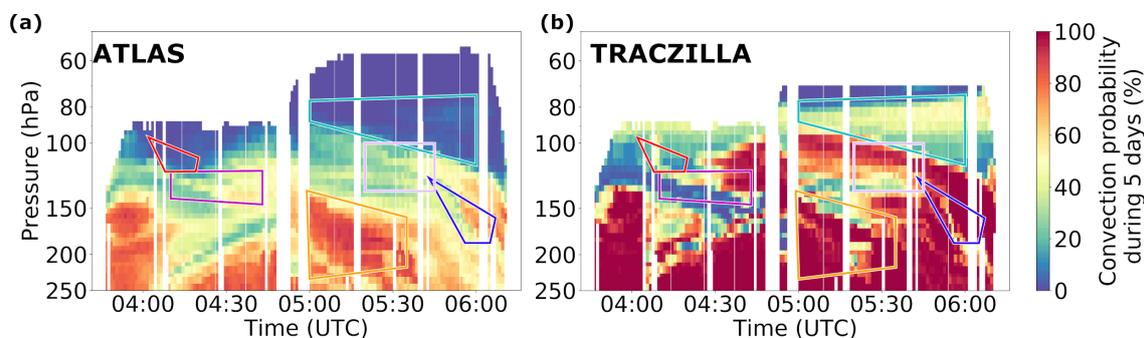
Figure 3. Convection probability of trajectories of the (a) ATLAS and (b) TRACZILLA model starting at the tangent points of the GLORIA measurements. The colors indicate the fraction of trajectories that experienced convection during the five days before the measurement time. Please note that the vertical axis is shown as pressure in logarithmic scale. For TRACZILLA, pressures below 70 hPa are not shown, as the convection detection with cloud top temperatures does not work in the stratosphere.

convection, which is usually not resolved in the reanalysis data used by the models, both models use advanced methods for the detection of convective events along the trajectories (see Secs. 2.3.3-2.3.4). Fig. 3 shows the fraction of trajectories for each GLORIA measurement time and location that experienced convection during the past 5 days. This fraction is interpreted as convection probability and aides the following interpretation of the origin of polluted air masses. The ATLAS trajectories

5 indicate an enhanced convection probability of more than 50% for the orange and blue marked regions, and parts of the purple and magenta regions also have convection probabilities of 50%, while the red and cyan regions show no noticeable enhancement of convection probability. For the TRACZILLA trajectories, the convection probabilities are overall higher, but as for ATLAS, the orange and blue region have highest convection probabilities, the purple and magenta region have parts with high convection probability, and the red and cyan regions have relatively low convection probabilities. These different absolute

10 percentages for convection probability for ATLAS and TRACZILLA are likely the result of the different methods for detection of convection along the backward trajectories by the models. Another region of enhanced convection probability below 15 km and earlier than 04:10 UTC is present in both models but not marked by any colored box. This is the part of the flight, where Höpfner et al. (2019) report strongly enhanced ammonia VMRs. In their paper, the same sets of trajectories are used to estimate the source of origin at the border region between Pakistan and India.

15 Fig. 4a shows exemplary backward trajectories from the ATLAS model released from the orange region of interest (as defined in Fig. 2 and following). Along these trajectories, regions are bordered orange, where the density of convective events along these trajectories is larger than 0.1%, 1.0%, and 10.0%. This density is calculated as the fraction of the number of convective events over the total number of released trajectories from this particular region on a 1° latitude × 1° longitude grid. I. e. the smallest bordered regions include at least 0.1% (or 1.0% and 10.0% for the inner lines) of convective events of

20 all released backward trajectories in a given color, while larger regions contain accordingly a larger fraction. These orange areas are repeated in Fig. 4b, together with the colored areas for the other regions of interest, as defined in Fig. 2. In the same manner, areas of high density of convective events calculated by TRACZILLA are shown for all colored regions, in Fig. 4c. In
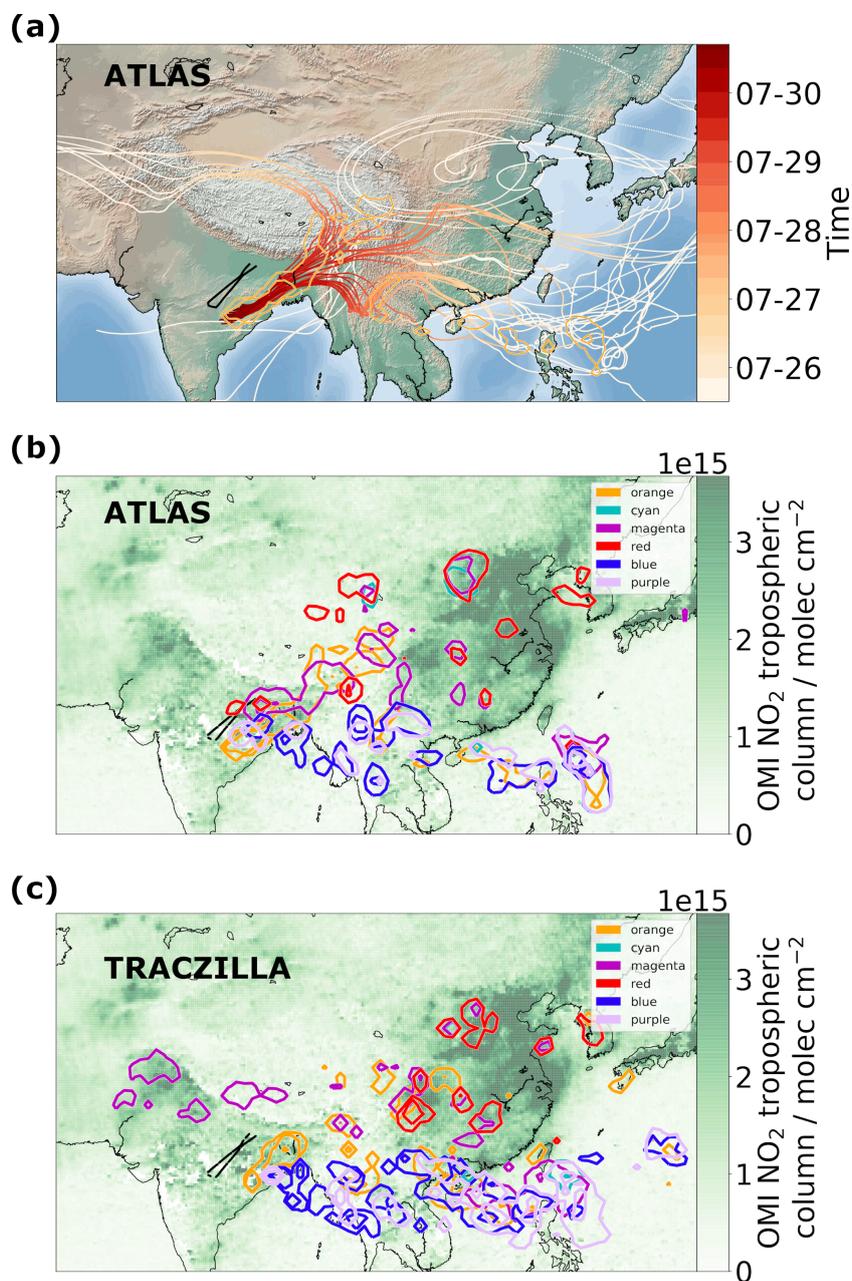
Figure 4. The origin of regions of interest along the GLORIA vertical cross sections. (a) Exemplary subset of backward ATLAS trajectories starting at the region marked orange in Figs. 2-3. Backward trajectories are displayed in this figure for 10 days of which the temporal evolution fo the first 5 days are color coded according to the color bar. Orange colored regions on the map mark regions, where the density of convective events (as explained in Sec. 2.3.4) is larger than 0.1%, 1.0%, and 10.0% (calculated as the number of encountered convective events over the number of total released trajectories; on a $1°$ latitude $\times$ $1°$ longitude grid). (b) Same regions as in (a), but for all colored regions from Figs. 2-3. Background: OMI satellite measurements of the tropospheric NO_2 column, averaged over 14 days before the measurement (c) Same as (b), but with density of convective events (as explained in Sec. 2.3.3) from TRACZILLA.

Fig. 4b,c, in addition, the OMI NO_2 tropospheric column is shown as average over 14 days prior to the measurement as a proxy for emission of polluted air masses. These averaged tropospheric NO_2 columns are shown as background in green colors.

The ATLAS and TRACZILLA models show partly different areas of convective events for the labeled regions of interest. In the following parts, the plausibility of the calculated areas of convective events is tested by comparing these regions to the OMI NO_2 tropospheric column:

- The red region of interest has been selected from the measurements due to enhanced pollution trace gas measurements during the first part of the flight, in contrast to the magenta region, which showed enhanced HNO_3, but otherwise a local minimum of pollutant species. For ATLAS and TRACZILLA, it was shown that only a small part of the trajectories experienced convection during 5 days before the measurement (see Fig. 3). In Fig. 4b-c, for both models regions are marked red between the location of the measurement and eastern China. As for most marked regions only the 0,1% lines are present, the convective influence along the trajectories was weak. However, red marked regions in north eastern China match to the enhanced NO_2 measurements and possibly contributed to the measured enhanced pollution trace gases. For the ATLAS model, it is shown in supplementary Fig. 12 that for backward trajectories from the red region less than 30% convective events occurred in these marked regions.

- The magenta region of interest is connected to a local minimum of PAN, C_2H_2 and HCOOH, and enhanced HNO_3, close to the red maximum. Both models show similar regions than for red above China, and in addition above the Southern Chinese and Philippine Sea. TRACZILLA also indicates regions north western of the flight path. Again, for almost all these marked regions only the 0,1% lines are present, which again indicates a low convective influence of the measured air masses. However, in case of convective contributions to these air masses, it is more likely that the regions above the Southern Chinese and Philippine Sea contributed with clean maritime air.

- The second part of the flight has again a region with enhanced NMVOC measurements, marked with orange color. Both models indicate that the trajectories encountered convection not too far away from the flight path. Between the flight path and the coast, even the 1%, and for TRACZILLA also the 10% lines are visible. This region is connected to enhanced OMI NO_2 measurements, which is a strong indication for local emissions from India. Smaller orange regions in both models, present above southern China and the Southern Chinese Sea, are not likely to contribute to the strongly enhanced measured pollutants. For the ATLAS model, it is shown in supplementary Fig. 14 that for backward trajectories from the orange region about 50% convective events occur spatially very close to the measurement location and within 3 days before the measurement. This corresponds to the more plausible orange region (according to the NO_2 columns), which seems to be more likely to contribute to the measured air masses according to supplementary Fig. 14.

- A local minimum of NMVOCs at the same altitude of measurement as the previous one is marked blue. Both models indicates regions between the flight path and the Bay of Bengal as source region, together with regions above Myanmar, and the South Chinese and Philippine Sea. All these regions show low NO_2 measurements and are therefore plausible source regions for the rather clean air masses measured by GLORIA.

– The local maximum of O_3 in the second part of the flight, below the tropopause is marked purple in the measurements (see Fig. 2). According to the convection along the model trajectories, the origin of these air masses is very similar to blue labeled air masses: Convection probabilities along the trajectories from the purple region are enhanced over west India and above the South Chinese and Philippine Sea.

5 – The cyan colored regions are connected to the measured enhancement of PAN and C_2H_2 above the tropopause. In Sec. 3, it is suggested that these air masses are transported for more than a few days, which indicates that convection 10 days before the measurement only had a minor influence to the transport of polluted air masses to the measurement geolocation. This is also supported by Fig. 3, which does not show enhanced convection probability in the cross sections, for both trajectory models. ATLAS and TRACZILLA both only show a region at the Philippine Sea for the cyan region of interest, and a region above central China. For the ATLAS model, it is shown in supplementary Fig. 17 that for backward trajectories from the cyan region less than 20% convective events of all trajectories occurred at all, which also indicates the low convective influence.

The comparison of ATLAS and TRACZILLA calculations of convective origin of the measured pollution species, shows that there are few differences between these model results. Both models indicate regions of origin that are plausible source regions 15 of pollutants, according to the OMI NO_2 measurements, while also both models indicate regions that are less plausible.

5   Comparison to model simulations

An application of our highly resolved measurements is shown in this section, in the evaluation of atmospheric models. Simulation results of the CAMS reanalysis and EMAC atmospheric models are interpolated onto the geolocations of the GLORIA measurements (see Fig. 1). Comparisons with the GLORIA measurements for each gas are shown in Fig. 5. Due to the rather 20 coarse horizontal resolution of the models, compared to the distance between GLORIA profiles, for these model comparisons the GLORIA cross sections have been averaged over 33 single profiles, i.e. a horizontal distance of approx. 100 km.

Comparisons of GLORIA HNO_3 with CAMS (Fig. 5a-b) show that no noticeable enhancements are simulated by the CAMS model. HNO_3 data are provided in the CAMS reanalysis data product, but the model does not include stratospheric chemistry and thus no stratospheric HNO_3. The comparison of the observations with EMAC HNO_3 (Fig. 5c) shows several similarities: 25 High stratospheric VMRs up to 2 ppbv are simulated above 19 km of the second part of the flight, that decrease to values of 0.75 ppbv at the tropopause. Maximum stratospheric values are not always simulated as high as measured, but agree within the GLORIA estimated error (see Supplement, Figs. 1 and 2). Delicate structures around the tropopause in the measurements are not repeated by the model, which can be explained with the lower horizontal resolution of EMAC. Below the tropopause, the diagonal structure in the first part of the flight (of which parts are in the magenta box) are reproduced by EMAC. In the model, 30 this structure continues into the second part of the flight, which has not been observed by GLORIA. This diagonal structure coincides with the gradient of EMAC PAN (see below), which suggests that this simulated tropospheric HNO_3 originates from
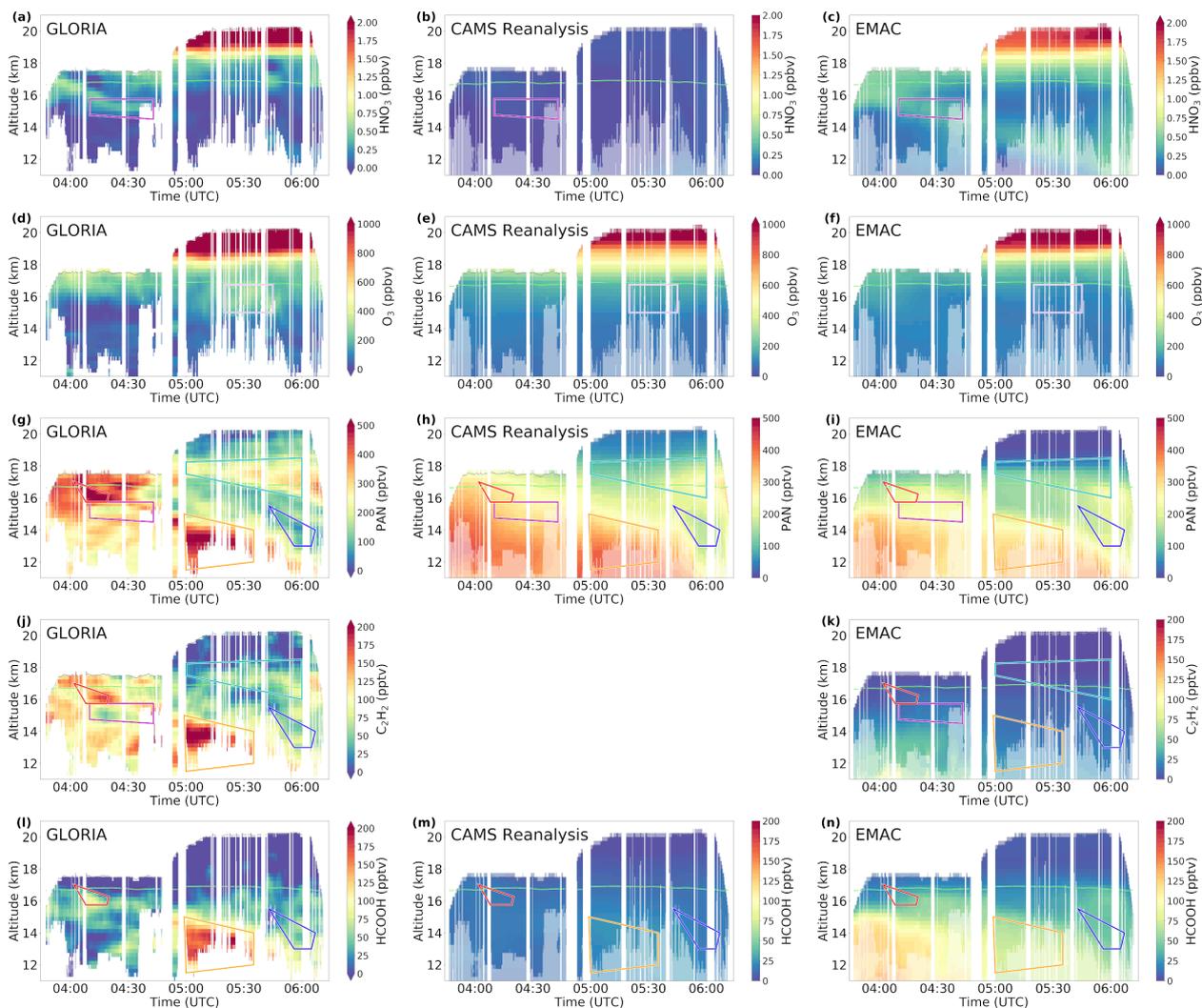
Figure 5. GLORIA (left column, similar to Fig. 2, but averaged over 33 single profiles), CAMS (middle column), and EMAC (right column) distributions of (a-c) HNO_3, (d-f) O_3, (g-i) PAN, (j-k) C_2H_2, (l-n) HCOOH for StratoClim flight on 31 July 2017. CAMS reanalysis does not include C_2H_2. All auxiliary lines as defined in caption of Fig. 2. Altitudes not measured by GLORIA are marked with a white shadow in the model data.

reactions with NO_2, product of the photolysis of PAN. Too high values below the tropopause are also simulated towards the end of the flight (6:00 UTC).

Comparisons between GLORIA O_3 and CAMS (Fig. 5d-e) show a general agreement between the two cross sections. In contrast to HNO_3, CAMS does have reasonable stratospheric values for O_3 due to a satellite data assimilation scheme, which 5 is only used for O_3. The general distribution of O_3 is also well reproduced by the EMAC model, which does not assimilate

satellite data, but applies a stratospheric chemistry scheme. Both models have difficulties to simulated the measured local enhancement at 5:30 UTC (purple box).

PAN is simulated similarly by CAMS and EMAC, and thus both models appear to have similar achievements and problems in reproducing the GLORIA measurements (Fig. 5g-i). The first part of the flight shows a local maximum (red box) above a
local minimum (magenta box), which is not simulated. Both models instead simulate a, more or less, constant decrease of PAN with altitude. In the second part of the flight, both models succeed to reproduce the location of relative maxima (orange and cyan boxes) and minimum (blue box), but not the absolute VMRs. While GLORIA measured more than 500 pptv of PAN in the orange box, CAMS simulates 400 pptv and EMAC not more than 300 pptv. The background values of tropospheric PAN are instead simulated higher (150 pptv) than measured (100 pptv). The measured enhancement above the tropopause (cyan box) is
only visible in the models towards the end of the flight and both models have lower maximum values (300 pptv for CAMS and 200 pptv for EMAC vs. 450 pptv for GLORIA).

C_2H_2 is only simulated by EMAC, which shows VMRs below 75 pptv, which is considerably below the measured VMRs (Fig. 5j-k). In the first part of the flight, EMAC simulates enhancements up to 50 pptv below 14 km, where also GLORIA measurements show a local maximum of up to 150 pptv C_2H_2. In the second part of the flight, again a very small enhancement
at the tropopause at 6:00 UTC is visible in EMAC, which is at the same geolocation as the enhancement in the measurements.

For HCOOH (Fig. 5l-n), CAMS only simulates VMRs below 50 pptv, which are measured as background values by GLO-RIA. The spatial distribution in CAMS shows a tiny enhancement up to 50 pptv close to the orange box, where GLORIA measured maximum values of more than 200 pptv. EMAC simulates HCOOH VMRs up to 125 pptv below 15 km altitude in the first part of the flight, where GLORIA measurements show no enhancements. The measured enhancement in the red box
is not reproduced by the model, but a local maximum is simulated at the same altitudes later during this flight (at 4:30 UTC). In the second part of the flight, the measured maximum (orange box) is simulated as a local maximum, but with considerably lower VMRs below 75 pptv.

These comparisons of GLORIA measurements with CAMS and EMAC show the limitations of atmospheric chemistry model simulations. In the first part of the flight, for all other gases than HNO_3, not even the structure was correctly simulated.
This indicates that the meteorological fields which prescribe transport in the simulations, do not include the processes relevant for the observed situation. Other explanations for the observed discrepancies between models and measurement are the source regions and emission strengths that are considered in the models. From Höpfner et al. (2019) it is known that air masses measured in this part of the flight have been influenced by convection over north-west India and northern Pakistan a few days before measurement. For that reason, a detailed analysis of trajectories is discussed in Sec. 4. In the second part of the flight,
models typically succeed to reproduce measured structures in the trace gases but with considerably lower absolute VMRs. This motivates the sensitivity study with EMAC in the next section, examining the influence of increased NMVOC emissions on the comparisons with GLORIA measurements. Further uncertainties in the models are errors within the concentrations of precursor species, uncertainties in or lack of implemented chemical reactions, temporal and spatial variability of the NMVOC emissions that are not considered by the emission inventories, and lack of or uncertainties in microphysical processes, such as
scavenging.
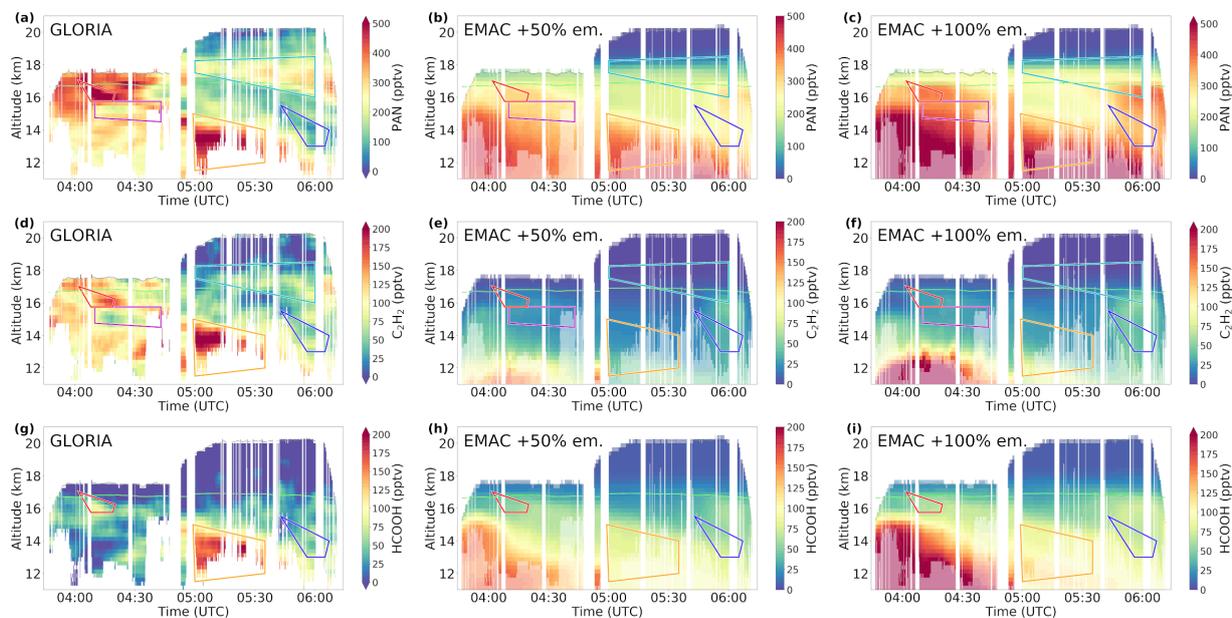
Figure 6. GLORIA (left column, repeated from Fig. 5, again averaged over 33 single profiles), EMAC with 50% (middle column), and EMAC with 100% increased NMVOC emissions (right column) distributions of (a-c) PAN, (d-f) C_2H_2, (g-i) HCOOH for StratoClim flight on 31 July 2017. All auxiliary lines as defined in caption of Fig. 2. Altitudes not measured by GLORIA are marked with a white shadow in the model data.

6   Influence of increased NMVOC emissions

In this section, the influence of increased NMVOC emissions as a possible source of uncertainty for the simulation results in the previous section is discussed for the EMAC model (see Fig. 6). Monks et al. (2018) suggest that NMVOC emissions are globally underestimated. As discussed in Sec. 5, it is expected that increased emissions improve the comparisons to GLORIA
5   measurements in the second part of the flight. During the first part of the flight, strong influence of convective events are suggested for altitudes up to 15 km. The comparison of this part of the flight is not expected to improve due to increased NMVOC emissions, and for that reason only the second part of the flight is discussed in detail here. As in the previous section, GLORIA results are presented as an average over 33 single profiles, to have comparable horizontal resolutions between measurement and model.

10   For PAN (Fig. 6a-c), the effect of increased NMVOC emissions is clearly visible in the comparison to the GLORIA measurements of the second part of the flight. Simulation results of the emission scenario "+100%" successfully reproduce measured PAN VMRs of more than 500 pptv in the orange box and of 300 pptv in the cyan box. However, in both these simulations with increased emissions, PAN background VMRs between the local maxima are too high in the simulation. E. g., in the blue box, more than 250 pptv ("+50%") and more than 350 pptv ("+100%") are simulated, while only less than 100 pptv are measured.

In contrast to PAN, increased NMVOC emissions in the EMAC model do not result in comparable C_2H_2 VMRs as in the measurement (Fig. 6d-f). In the orange box, more than 200 pptv of C_2H_2 are measured, while only less than 75 pptv are simulated in the "+100%" emission scenario. This is the same for enhancements at the tropopause (cyan box), where 100 pptv of C_2H_2 are measured and only 50 pptv simulated towards the end of the flight.

5   The measured maximum of HCOOH of more than 200 pptv (orange box) is also not reproduced by the "+100%" emission scenario of the EMAC simulation, which only results in up to 125 pptv in the orange box (Fig. 6g-i). As already observed in the EMAC simulation without enhanced emissions (see Fig. 5n), an enhancement of HCOOH at 6:00 UTC and 16 km altitude becomes more visible with increasing emissions, which is not observed by GLORIA.

    These comparisons of GLORIA measurements with EMAC simulations with increased NMVOC emissions show that for

10 PAN, the increased NMVOC emissions improve the comparison of the simulated maximum values to the measurements. The measured maximum VMRs are better reproduced by EMAC with the "+100%" emission scenario. Anyhow, the tropospheric background values are modeled too high in both, the "+50%" and "+100%", simulation. This is possibly caused by the limited resolution of the EMAC results. The GLORIA observations have higher vertical resolutions compared to EMAC and thus are able to resolve strong vertical gradients that EMAC can only reproduce on average and therefore smooths the finer resolved

15 image. The measured VMR distributions of C_2H_2 and HCOOH are not even reproduced by the EMAC run with 100% increased NMVOC emissions. This suggests that there are possibly other emission sources than in the emission inventory used by EMAC. Another explanation could be that emissions are not transported to the measurement geolocation as efficiently in the model as in reality. This also indicates convective events that are not resolved in the meteorological fields that are prescribing dynamics in EMAC. However, the overall structure of the simulated trace gases did not change due to the enhanced NMVOC emissions and

20 therefore other uncertainties in the simulation (as discussed in Sec.5) are considered to influence these structural differences between measurement and model.

7   Conclusions

This study discusses the first measurements of HNO_3, O_3, PAN, C_2H_2, and HCOOH in the center of the AMA UTLS. The observations reveal regions with strongly enhanced mixing ratios of these pollutants with maximum VMRs of more than

25 500 pptv for PAN, and more than 200 pptv of C_2H_2 and HCOOH. In particular, a layer of enhanced PAN ($\approx$400 pptv) and C_2H_2 ($\approx$100 pptv) has been measured at and above the tropopause. From the atmospheric lifetimes and the trajectory analysis, it is estimated that these enhancements exist in the atmosphere for longer than a few days. Other air masses below 15 km with strongly enhanced pollution trace gases measured are linked to recent convective events as transport mechanism to the upper troposphere. These measurements and their analysis show that PAN, a precursor of O_3, is efficiently transported upwards by

30 convection, and transported for a longer time in the tropopause region. In contrast to the study by Gottschaldt et al. (2018), no enhancements of O_3 are visible in our measurements. However, the enhancements discussed by Gottschaldt et al. (2018) are within the estimated observational uncertainty and, thus, cannot be ruled out.

We found indications that HCOOH was washed out, while in the same air masses PAN, C_2H_2 and also water soluble NH_3 was transported to the measurement geolocation. From Höpfner et al. (2019), it is reported that a large amount of up to 1 ppbv of NH_3 was measured at the same air masses of the HCOOH minimum. Because IASI satellite total column measurements show for both species, HCOOH and NH_3 maxima at the estimated area of origin of these air masses (according to Höpfner et al., 2019), it is suggested that the wash out process in this air masses was very different for these species, due to their different Henry constants and the pH of the droplets. However, we cannot rule out other processes leading to the different behavior of HCOOH and NH3 upon transport to the UT, like a difference in retention of those gases upon freezing of the liquid water droplets at high altitudes (Ge et al., 2018). At later measurements during the flight for air masses of different origin and history, it is shown that enhanced HCOOH VMRs up to 200 pptv can reach altitudes up to 15 km without being washed out.

The analysis of backward trajectories from ATLAS and TRACZILLA shows that the two methods for the treatment of convection of these models highlight similar regions of enhanced convective upward transport. Backward trajectories, starting at the geolocations of measurements with local maxima and minima of NMVOCs, indicate various regions of enhanced convection and thus of the origin of these air masses. Air masses with enhanced PAN, C_2H_2 and HCOOH at altitudes between 12 and 15 km in the second part of the flight are connected with convection over India, while unpolluted air masses at similar altitudes are connected with convection events over sea and coastal areas. A comparison of these indicated regions with measured OMI NO_2 enhancements indicate that some of these regions are plausible pollution sources. Similarly to Bucci et al. (2020), we find a strong convective influence of the transport of polluted air masses to the upper troposphere.

Comparisons of the measurements to CAMS and EMAC simulation results show that the first part of the flight appears to be under high convective influence, which the models do not account for. In the second part of the flight, CAMS and EMAC reproduce large scale structures of the spatial distributions of the measured trace gases, while the simulated VMRs are considerably lower compared to the measurements. We have performed a sensitivity study with EMAC with enhanced NMVOC emissions, increased by 50% and 100%. With the increased NMVOC emissions, the simulations show similar maximum values for PAN compared to GLORIA, but tropospheric background VMRs are simulated considerably too high. These too high background VMRs are attributed at least partly to the spatial resolution of EMAC, which does not resolve structures as fine as measured by GLORIA due to numerical diffusion in the model. EMAC simulations of C_2H_2 and HCOOH do not reproduce the strong enhancements in the second part of the flight, even with emissions increased by 100%. Therefore other uncertainties in the model apparently play a greater role: The emissions used in the model might not reproduce the temporal and spatial variability, convection events are not covered by the meteorological fields and the T106 horizontal resolution still is rather course for these highly resolved measurements by GLORIA.

In our paper, we show that there are very delicate structures and a large variability of pollutant trace gases over horizontal scales of 200 km in the Asian monsoon UTLS. Some enhancements have been transported into the upper troposphere by convection within days before the measurements, while one measured region has been transported around the tropopause and lowermost stratosphere for a longer time. Atmospheric models have difficulties in reproducing these structures and explaining the origin of the measured species, which is likely to be caused by uncertainties of the prescribed NMVOC emissions, rather coarse model resolution, and insufficient vertical transport from convection in meteorological fields. Advanced schemes for

convection detection along backward trajectories allow for an estimation of origin for the polluted air masses measured by GLORIA.

Data availability. GLORIA measurements are available in the database HALO-DB (https://halo-db.pa.op.dlr.de/mission/101) and will be available on the KITopen repository. The CAMS model data is available from ECMWF (https://apps.ecmwf.int/data-catalogues/cams-reanalysis).
5 OMI NO_2 level 3 data is available from NASA (Krotkov, 2013, https://doi.org/10.5067/Aura/OMI/DATA3007). The EMAC, ATLAS and TRACZILLA data are available upon request.

Author contributions. SJ initiated the study, performed the analyses, and wrote the manuscript. MH, JU, GW, NG and SJ performed the GLORIA data processing. FFV and EK operated GLORIA during the StratoClim campaign in Kathmandu. OK performed the EMAC simulations and designed the sensitivity studies. SB and BL performed the TRACZILLA trajectory simulations. IW performed the ATLAS
10 trajectory simulations. All authors commented on and improved the manuscript.

Competing interests. The authors declare that they have no conflict of interest.

Acknowledgements. We gratefully thank the StratoClim coordination team, in particular Fred Stroh, and Myasishchev Design Bureau for successfully conducting the field campaign. The results are based on the efforts of all members of the GLORIA team, including the technology institutes ZEA-1 and ZEA-2 at Forschungszentrum Jülich and the Institute for Data Processing and Electronics at the Karlsruhe Institute of
15 Technology. We thank ECMWF for providing CAMS data and NASA for providing OMI data. The EMAC simulations were performed on the supercomputer ForHLR funded by the Ministry of Science, Research and the Arts Baden-Württemberg and by the Federal Ministry of Education and Research.

Sören Johansson has received funding from the European Community's Seventh Framework Programme (FP7/2007–2013) under grant agreement 603557. We acknowledge support by the Deutsche Forschungsgemeinschaft and the Open Access Publishing Fund of the Karl-
20 sruhe Institute of Technology.

References

Basha, G., Ratnam, M. V., Kishore, P., Ravindrababu, S., and Velicogna, I.: Influence of Asian Summer Monsoon Anticyclone on the Trace gases and Aerosols over Indian region, Atmospheric Chemistry and Physics Discussions, pp. 1–33, https://www.atmos-chem-phys-discuss.net/acp-2019-743/acp-2019-743.pdf, 2019.

5 Bian, J., Pan, L. L., Paulik, L., Vömel, H., Chen, H., and Lu, D.: In situ water vapor and ozone measurements in Lhasa and Kunming during the Asian summer monsoon, Geophysical Research Letters, 39, https://agupubs.onlinelibrary.wiley.com/doi/pdf/10.1029/2012GL052996, 2012.

Brasseur, G. and Solomon, S.: Aeronomy of the middle atmosphere: Chemistry and physics of the stratosphere and mesosphere, vol. 32 of *Atmospheric and oceanographic sciences library*, Springer, Dordrecht and [Great Britain], 3rd rev. and enl. edn., 2005.

10 Braun, M., Grooß, J.-U., Woiwode, W., Johansson, S., Höpfner, M., Friedl-Vallon, F., Oelhaf, H., Preusse, P., Ungermann, J., Sinnhuber, B.-M., Ziereis, H., and Braesicke, P.: Nitrification of the lowermost stratosphere during the exceptionally cold Arctic winter 2015–2016, Atmospheric Chemistry and Physics, 19, 13 681–13 699, https://www.atmos-chem-phys.net/19/13681/2019/acp-19-13681-2019.pdf, 2019.

Browell, E. V., Danielsen, E. F., Ismail, S., Gregory, G. L., and Beck, S. M.: Tropopause fold structure determined from airborne lidar and in situ measurements, Journal of Geophysical Research, 92, 2112, 1987.

15 Brunamonti, S., Jorge, T., Oelsner, P., Hanumanthu, S., Singh, B. B., Kumar, K. R., Sonbawne, S., Meier, S., Singh, D., Wienhold, F. G., Luo, B. P., Boettcher, M., Poltera, Y., Jauhiainen, H., Kayastha, R., Karmacharya, J., Dirksen, R., Naja, M., Rex, M., Fadnavis, S., and Peter, T.: Balloon-borne measurements of temperature, water vapor, ozone and aerosol backscatter on the southern slopes of the Himalayas during StratoClim 2016–2017, Atmospheric Chemistry and Physics, 18, 15 937–15 957, https://www.atmos-chem-phys.net/18/15937/2018/acp-18-15937-2018.pdf, 2018.

20 Bucci, S., Legras, B., Sellitto, P., D'Amato, F., Viciani, S., Montori, A., Chiarugi, A., Ravegnani, F., Ulanovsky, A., Cairo, F., and Stroh, F.: Deep convective influence on the UTLS composition in the Asian Monsoon Anticyclone region: 2017 StratoClim campaign results, Atmospheric Chemistry and Physics Discussions, pp. 1–29, https://www.atmos-chem-phys-discuss.net/acp-2019-1053/acp-2019-1053.pdf, 2020.

Burkholder, J. B., Sander, S. P., Abbatt, J., Barker, J. R., Huie, R. E., Kolb, C. E., Kurylo, M. J., Orkin, V. L., Wilmouth, D. M., and 25 Wine, P. H.: Chemical Kinetics and Photochemical Data for Use in Atmospheric Studies, Evaluation No. 18, JPL Publication, 15-10, http://jpldataeval.jpl.nasa.gov, 2015.

Coheur, P.-F., Herbin, H., Clerbaux, C., Hurtmans, D., Wespes, C., Carleer, M., Turquety, S., Rinsland, C. P., Remedios, J., Hauglustaine, D., Boone, C. D., and Bernath, P. F.: ACE-FTS observation of a young biomass burning plume: First reported measurements of C_2H_4, C_3H_6O, H_2CO and PAN by infrared occultation from space, Atmospheric Chemistry and Physics, 7, 5437–5446, https://www.atmos-chem-phys. 30 net/7/5437/2007/acp-7-5437-2007.pdf, 2007.

Coheur, P.-F., Clarisse, L., Turquety, S., Hurtmans, D., and Clerbaux, C.: IASI measurements of reactive trace species in biomass burning plumes, Atmospheric Chemistry and Physics, 9, 5655–5667, https://www.atmos-chem-phys.net/9/5655/2009/acp-9-5655-2009.pdf, 2009.

Crutzen, P. J.: The role of NO and NO2 in the chemistry of the troposphere and stratosphere, Annual review of earth and planetary sciences, 7, 443–472, 1979.

35 Cussac, M., Marécal, V., Thouret, V., Josse, B., and Sauvage, B.: The impact of biomass burning on upper tropospheric carbon monoxide: A study using MOCAGE global model and IAGOS airborne data, Atmospheric Chemistry and Physics Discussions, pp. 1–32, https://www.atmos-chem-phys-discuss.net/acp-2019-1143/acp-2019-1143.pdf, 2020.

Dee, D. P., Uppala, S. M., Simmons, A. J., Berrisford, P., Poli, P., Kobayashi, S., Andrae, U., Balmaseda, M. A., Balsamo, G., Bauer, P., Bechtold, P., Beljaars, A. C. M., van de Berg, L., Bidlot, J., Bormann, N., Delsol, C., Dragani, R., Fuentes, M., Geer, A. J., Haimberger, L., Healy, S. B., Hersbach, H., Hólm, E. V., Isaksen, L., Kållberg, P., Köhler, M., Matricardi, M., McNally, A. P., Monge-Sanz, B. M., Morcrette, J., Park, B., Peubey, C., Rosnay, P. d., Tavolato, C., Thépaut, J., and Vitart, F.: The ERA-Interim reanalysis: configuration and performance of the data assimilation system, Quarterly Journal of the Royal Meteorological Society, 137, 553–597, https://rmets.onlinelibrary.wiley.com/doi/pdf/10.1002/qj.828, 2011.

Derrien, M., Le Gleau, H., and Raoul, M.-P.: The use of the high resolution visible in SAFNWC/MSG cloud mask, https://hal-meteofrance.archives-ouvertes.fr/meteo-00604325/document, 2010.

Fadnavis, S., Schultz, M. G., Semeniuk, K., Mahajan, A. S., Pozzoli, L., Sonbawne, S., Ghude, S. D., Kiefer, M., and Eckert, E.: Trends in peroxyacetyl nitrate (PAN) in the upper troposphere and lower stratosphere over southern Asia during the summer monsoon season: regional impacts, Atmospheric Chemistry and Physics, 14, 12 725–12 743, 2014.

Fischer, E. V., Jacob, D. J., Yantosca, R. M., Sulprizio, M. P., Millet, D. B., Mao, J., Paulot, F., Singh, H. B., Roiger, A., Ries, L., Talbot, R. W., Dzepina, K., and Pandey Deolal, S.: Atmospheric peroxyacetyl nitrate (PAN): A global budget and source attribution, Atmospheric Chemistry and Physics, 14, 2679–2698, https://www.atmos-chem-phys.net/14/2679/2014/acp-14-2679-2014.pdf, 2014.

Flemming, J., Huijnen, V., Arteta, J., Bechtold, P., Beljaars, A., Blechschmidt, A.-M., Diamantakis, M., Engelen, R. J., Gaudel, A., Inness, A., Jones, L., Josse, B., Katragkou, E., Marecal, V., Peuch, V.-H., Richter, A., Schultz, M. G., Stein, O., and Tsikerdekis, A.: Tropospheric chemistry in the Integrated Forecasting System of ECMWF, Geoscientific Model Development, 8, 975–1003, https://www.geosci-model-dev.net/8/975/2015/gmd-8-975-2015.pdf, 2015.

Friedl-Vallon, F., Gulde, T., Hase, F., Kleinert, A., Kulessa, T., Maucher, G., Neubert, T., Olschewski, F., Piesch, C., Preusse, P., Rongen, H., Sartorius, C., Schneider, H., Schönfeld, A., Tan, V., Bayer, N., Blank, J., Dapp, R., Ebersoldt, A., Fischer, H., Graf, F., Guggenmoser, T., Höpfner, M., Kaufmann, M., Kretschmer, E., Latzko, T., Nordmeyer, H., Oelhaf, H., Orphal, J., Riese, M., Schardt, G., Schillings, J., Sha, M. K., Suminska-Ebersoldt, O., and Ungermann, J.: Instrument concept of the imaging Fourier transform spectrometer GLORIA, Atmospheric Measurement Techniques, 7, 3565–3577, 2014.

Froidevaux, L., Waters, J. W., Read, W. G., Elson, L. S., Flower, D. A., and Jarnot, R. F.: Global Ozone Observations from the UARS MLS: An Overview of Zonal-Mean Results, Journal of the Atmospheric Sciences, 51, 2846–2866, 1994.

Ge, C., Zhu, C., Francisco, J. S., Zeng, X. C., and Wang, J.: A molecular perspective for global modeling of upper atmospheric NH3 from freezing clouds, Proceedings of the National Academy of Sciences, 115, 6147–6152, https://www.pnas.org/content/115/24/6147, 2018.

Glatthor, N., von Clarmann, T., Fischer, H., Funke, B., Grabowski, U., Höpfner, M., Kellmann, S., Kiefer, M., Linden, A., Milz, M., Steck, T., and Stiller, G. P.: Global peroxyacetyl nitrate (PAN) retrieval in the upper troposphere from limb emission spectra of the Michelson Interferometer for Passive Atmospheric Sounding (MIPAS), Atmospheric Chemistry and Physics, 7, 2775–2787, https://www.atmos-chem-phys.net/7/2775/2007/acp-7-2775-2007.pdf, 2007.

Gottschaldt, K.-D., Schlager, H., Baumann, R., Cai, D. S., Eyring, V., Graf, P., Grewe, V., Jöckel, P., Jurkat-Witschas, T., Voigt, C., Zahn, A., and Ziereis, H.: Dynamics and composition of the Asian summer monsoon anticyclone, Atmospheric Chemistry and Physics, 18, 5655–5675, https://www.atmos-chem-phys.net/18/5655/2018/acp-18-5655-2018.pdf, 2018.

Grutter, M., Glatthor, N., Stiller, G. P., Fischer, H., Grabowski, U., Höpfner, M., Kellmann, S., Linden, A., and von Clarmann, T.: Global distribution and variability of formic acid as observed by MIPAS-ENVISAT, Journal of Geophysical Research: Atmospheres, 115, https://agupubs.onlinelibrary.wiley.com/doi/full/10.1029/2009JD012980, 2010.

Höpfner, M., Volkamer, R., Grabowski, U., Grutter, M., Orphal, J., Stiller, G., Clarmann, T. V., and Wetzel, G.: First detection of ammonia (NH_3) in the Asian summer monsoon upper troposphere, Atmospheric Chemistry and Physics, 16, 14 357–14 369, https://www.atmos-chem-phys.net/16/14357/2016/acp-16-14357-2016.pdf, 2016.

Höpfner, M., Ungermann, J., Borrmann, S., Wagner, R., Spang, R., Riese, M., Stiller, G., Appel, O., Batenburg, A. M., Bucci, S., Cairo, F., Dragoneas, A., Friedl-Vallon, F., Hünig, A., Johansson, S., Krasauskas, L., Legras, B., Leisner, T., Mahnke, C., Möhler, O., Molleker, S., Müller, R., Neubert, T., Orphal, J., Preusse, P., Rex, M., Saathoff, H., Stroh, F., Weigel, R., and Wohltmann, I.: Ammonium nitrate particles formed in upper troposphere from ground ammonia sources during Asian monsoons, Nature Geoscience, 12, 608–612, 2019.

Inness, A., Ades, M., Agustí-Panareda, A., Barré, J., Benedictow, A., Blechschmidt, A.-M., Dominguez, J. J., Engelen, R., Eskes, H., Flemming, J., Huijnen, V., Jones, L., Kipling, Z., Massart, S., Parrington, M., Peuch, V.-H., Razinger, M., Remy, S., Schulz, M., and Suttie, M.: The CAMS reanalysis of atmospheric composition, Atmospheric Chemistry and Physics, 19, 3515–3556, https://www.atmos-chem-phys.net/19/3515/2019/acp-19-3515-2019.pdf, 2019.

James, R., Bonazzola, M., Legras, B., Surbled, K., and Fueglistaler, S.: Water vapor transport and dehydration above convective outflow during Asian monsoon, Geophysical Research Letters, 35, https://agupubs.onlinelibrary.wiley.com/doi/pdf/10.1029/2008GL035441, 2008.

Jöckel, P., Kerkweg, A., Pozzer, A., Sander, R., Tost, H., Riede, H., Baumgaertner, A., Gromov, S., and Kern, B.: Development cycle 2 of the Modular Earth Submodel System (MESSy2), Geoscientific Model Development, 3, 717–752, https://www.geosci-model-dev.net/3/717/2010/gmd-3-717-2010.pdf, 2010.

Johansson, S., Woiwode, W., Höpfner, M., Friedl-Vallon, F., Kleinert, A., Kretschmer, E., Latzko, T., Orphal, J., Preusse, P., Ungermann, J., Santee, M. L., Jurkat-Witschas, T., Marsing, A., Voigt, C., Giez, A., Krämer, M., Rolf, C., Zahn, A., Engel, A., Sinnhuber, B.-M., and Oelhaf, H.: Airborne limb-imaging measurements of temperature, HNO3, O3, ClONO2, H2O and CFC-12 during the Arctic winter 2015/2016: Characterization, in situ validation and comparison to Aura/MLS, Atmospheric Measurement Techniques, 11, 4737–4756, https://www.atmos-meas-tech.net/11/4737/2018/amt-11-4737-2018.pdf, 2018.

Jurkat, T., Kaufmann, S., Voigt, C., Schäuble, D., Jeßberger, P., and Zireis, H.: The airborne mass spectrometer AIMS – Part 2: Measurements of trace gases with stratospheric or tropospheric origin in the UTLS, Atmospheric Measurement Techniques, 9, 1907–1923, https://www.atmos-meas-tech.net/9/1907/2016/amt-9-1907-2016.pdf, 2016.

Krotkov, N. A.: OMI/Aura NO2 Cloud-Screened Total and Tropospheric Column Daily L3 Global 0.25deg Lat/Lon Grid, 2013.

Legras, B. and Bucci, S.: Confinement of air in the Asian monsoon anticyclone and pathways of convective air to the stratosphere during summer season, Atmospheric Chemistry and Physics Discussions, pp. 1–37, https://www.atmos-chem-phys-discuss.net/acp-2019-1075/acp-2019-1075.pdf, 2019.

Legras, B., Pisso, I., Berthet, G., and Lefèvre, F.: Variability of the Lagrangian turbulent diffusion in the lower stratosphere, Atmospheric Chemistry and Physics, 5, 1605–1622, https://www.atmos-chem-phys.net/5/1605/2005/acp-5-1605-2005.pdf, 2005.

Lelieveld, J., Bourtsoukidis, E., Brühl, C., Fischer, H., Fuchs, H., Harder, H., Hofzumahaus, A., Holland, F., Marno, D., Neumaier, M., Pozzer, A., Schlager, H., Williams, J., Zahn, A., and Zireis, H.: The South Asian monsoon—pollution pump and purifier, Science, 361, 270–273, https://science.sciencemag.org/content/sci/361/6399/270.full.pdf, 2018.

Levelt, P. F., van den Oord, G., Dobber, M. R., Malkki, A., Visser, H., Vries, J. d., Stammes, P., Lundell, J., and Saari, H.: The ozone monitoring instrument, IEEE Transactions on Geoscience and Remote Sensing, 44, 1093–1101, 2006.

Li, D., Vogel, B., Müller, R., Bian, J., Günther, G., Li, Q., Zhang, J., Bai, Z., Vömel, H., and Riese, M.: High tropospheric ozone in Lhasa within the Asian summer monsoon anticyclone in 2013: influence of convective transport and stratospheric intrusions, Atmospheric Chemistry and Physics, 18, 17 979–17 994, https://www.atmos-chem-phys.net/18/17979/2018/acp-18-17979-2018.pdf, 2018.

Livesey, N. J., Filipiak, M. J., Froidevaux, L., Read, W. G., Lambert, A., Santee, M. L., Jiang, J. H., Pumphrey, H. C., Waters, J. W., Cofield, R. E., Cuddy, D. T., Daffer, W. H., Drouin, B. J., Fuller, R. A., Jarnot, R. F., Jiang, Y. B., Knosp, B. W., Li, Q. B., Perun, V. S., Schwartz, M. J., Snyder, W. V., Stek, P. C., Thurstans, R. P., Wagner, P. A., Avery, M., Browell, E. V., Cammas, J., Christensen, L. E., Diskin, G. S., Gao, R., Jost, H., Loewenstein, M., Lopez, J. D., Nedelec, P., Osterman, G. B., Sachse, G. W., and Webster, C. R.: Validation of Aura Microwave Limb Sounder O3 and CO observations in the upper troposphere and lower stratosphere, Journal of Geophysical Research: Atmospheres, 113, https://agupubs.onlinelibrary.wiley.com/doi/full/10.1029/2007JD008805, 2008.

Millet, D. B., Baasandorj, M., Farmer, D. K., Thornton, J. A., Baumann, K., Brophy, P., Chaliyakunnel, S., Gouw, J. A. d., Graus, M., Hu, L., Koss, A., Lee, B. H., Lopez-Hilfiker, F. D., Neuman, J. A., Paulot, F., Peischl, J., Pollack, I. B., Ryerson, T. B., Warneke, C., Williams, B. J., and Xu, J.: A large and ubiquitous source of atmospheric formic acid, Atmospheric Chemistry and Physics, 15, 6283–6304, https://www.atmos-chem-phys.net/15/6283/2015/acp-15-6283-2015.pdf, 2015.

Monks, S. A., Wilson, C., Emmons, L. K., Hannigan, J. W., Helmig, D., Blake, N. J., and Blake, D. R.: Using an Inverse Model to Reconcile Differences in Simulated and Observed Global Ethane Concentrations and Trends Between 2008 and 2014, Journal of Geophysical Research: Atmospheres, 123, 11,262–11,282, https://agupubs.onlinelibrary.wiley.com/doi/full/10.1029/2017JD028112, 2018.

Morcrette, J., Boucher, O., Jones, L., Salmond, D., Bechtold, P., Beljaars, A., Benedetti, A., Bonet, A., Kaiser, J. W., Razinger, M., Schulz, M., Serrar, S., Simmons, A. J., Sofiev, M., Suttie, M., Tompkins, A. M., and Untch, A.: Aerosol analysis and forecast in the European Centre for Medium-Range Weather Forecasts Integrated Forecast System: Forward modeling, Journal of Geophysical Research: Atmospheres, 114, https://agupubs.onlinelibrary.wiley.com/doi/pdf/10.1029/2008JD011235, 2009.

Mungall, E. L., Abbatt, J. P. D., Wentzell, J. J. B., Wentworth, G. R., Murphy, J. G., Kunkel, D., Gute, E., Tarasick, D. W., Sharma, S., Cox, C. J., Uttal, T., and Liggio, J.: High gas-phase mixing ratios of formic and acetic acid in the High Arctic, Atmospheric Chemistry and Physics, 18, 10 237–10 254, https://www.atmos-chem-phys.net/18/10237/2018/acp-18-10237-2018.pdf, 2018.

Neuman, J. A., Gao, R. S., Fahey, D. W., Holecek, J. C., Ridley, B. A., Walega, J. G., Grahek, F. E., Richard, E. C., McElroy, C. T., Thompson, T. L., Elkins, J. W., Moore, F. L., and Ray, E. A.: In situ measurements of HNO3, NOy, NO, and O3 in the lower stratosphere and upper troposphere, Atmospheric Environment, 35, 5789–5797, 2001.

Pan, L. L., Honomichl, S. B., Kinnison, D. E., Abalos, M., Randel, W. J., Bergman, J. W., and Bian, J.: Transport of chemical tracers from the boundary layer to stratosphere associated with the dynamics of the Asian summer monsoon, Journal of Geophysical Research: Atmospheres, 121, 14,159–14,174, https://agupubs.onlinelibrary.wiley.com/doi/full/10.1002/2016JD025616, 2016.

Park, M., Randel, W. J., Gettelman, A., Massie, S. T., and Jiang, J. H.: Transport above the Asian summer monsoon anticyclone inferred from Aura Microwave Limb Sounder tracers, Journal of Geophysical Research, 112, 253, 2007.

Park, M., Randel, W. J., Emmons, L. K., Bernath, P. F., Walker, K. A., and Boone, C. D.: Chemical isolation in the Asian monsoon anticyclone observed in Atmospheric Chemistry Experiment (ACE-FTS) data, Atmospheric Chemistry and Physics, 8, 757–764, 2008.

Paulot, F., Wunch, D., Crounse, J. D., Toon, G. C., Millet, D. B., DeCarlo, P. F., Vigouroux, C., Deutscher, N. M., González Abad, G., Notholt, J., Warneke, T., Hannigan, J. W., Warneke, C., Gouw, J. A. d., Dunlea, E. J., Mazière, M. D., Griffith, D. W. T., Bernath, P., Jimenez, J. L., and Wennberg, P. O.: Importance of secondary sources in the atmospheric budgets of formic and acetic acids, Atmospheric Chemistry and Physics, 11, 1989–2013, https://www.atmos-chem-phys.net/11/1989/2011/acp-11-1989-2011.pdf, 2011.

Pisso, I. and Legras, B.: Turbulent vertical diffusivity in the sub-tropical stratosphere, Atmospheric Chemistry and Physics, 8, 697–707, https://www.atmos-chem-phys.net/8/697/2008/acp-8-697-2008.pdf, 2008.

Randel, W. J. and Jensen, E. J.: Physical processes in the tropical tropopause layer and their roles in a changing climate, Nature Geoscience, 6, 169–176, https://www.nature.com/articles/ngeo1733.pdf, 2013.

Reiner, T., Möhler, O., and Arnold, F.: Measurements of acetone, acetic acid, and formic acid in the northern midlatitude upper troposphere and lower stratosphere, Journal of Geophysical Research: Atmospheres, 104, 13 943–13 952, https://agupubs.onlinelibrary.wiley.com/doi/full/10.1029/1999JD900030, 1999.

Riese, M., Oelhaf, H., Preusse, P., Blank, J., Ern, M., Friedl-Vallon, F., Fischer, H., Guggenmoser, T., Höpfner, M., Hoor, P., Kaufmann, M., Orphal, J., Plöger, F., Spang, R., Suminska-Ebersoldt, O., Ungermann, J., Vogel, B., and Woiwode, W.: Gimballed Limb Observer for Radiance Imaging of the Atmosphere (GLORIA) scientific objectives, Atmospheric Measurement Techniques, 7, 1915–1928, 2014.

Rinsland, C. P., Zander, R., Farmer, C. B., Norton, R. H., and Russell, J. M.: Concentrations of ethane (C2H6) in the lower stratosphere and upper troposphere and acetylene (C2H2) in the upper troposphere deduced from atmospheric trace molecule spectroscopy/Spacelab 3 spectra, Journal of Geophysical Research: Atmospheres, 92, 11 951–11 964, https://agupubs.onlinelibrary.wiley.com/doi/full/10.1029/JD092iD10p11951, 1987.

Rinsland, C. P., Dufour, G., Boone, C. D., Bernath, P. F., and Chiou, L.: Atmospheric Chemistry Experiment (ACE) measurements of elevated Southern Hemisphere upper tropospheric CO, C2H6, HCN, and C2H2 mixing ratios from biomass burning emissions and long-range transport, Geophysical Research Letters, 32, https://agupubs.onlinelibrary.wiley.com/doi/full/10.1029/2005GL024214, 2005.

Rinsland, C. P., Boone, C. D., Bernath, P. F., Mahieu, E., Zander, R., Dufour, G., Clerbaux, C., Turquety, S., Chiou, L., McConnell, J. C., Neary, L., and Kaminski, J. W.: First space-based observations of formic acid (HCOOH): Atmospheric Chemistry Experiment austral spring 2004 and 2005 Southern Hemisphere tropical-mid-latitude upper tropospheric measurements, Geophysical Research Letters, 33, https://agupubs.onlinelibrary.wiley.com/doi/full/10.1029/2006GL027128, 2006.

Roeckner, E., Brokopf, R., Esch, M., Giorgetta, M., Hagemann, S., Kornblueh, L., Manzini, E., Schlese, U., and Schulzweida, U.: Sensitivity of Simulated Climate to Horizontal and Vertical Resolution in the ECHAM5 Atmosphere Model, Journal of Climate, 19, 3771–3791, 2006.

Safieddine, S., Boynard, A., Hao, N., Huang, F., Wang, L., Ji, D., Barret, B., Ghude, S. D., Coheur, P.-F., Hurtmans, D., and Clerbaux, C.: Tropospheric ozone variability during the East Asian summer monsoon as observed by satellite (IASI), aircraft (MOZAIC) and ground stations, Atmospheric Chemistry and Physics, 16, 10 489–10 500, https://www.atmos-chem-phys.net/16/10489/2016/acp-16-10489-2016.pdf, 2016.

Sander, R., Baumgaertner, A., Gromov, S., Harder, H., Jöckel, P., Kerkweg, A., Kubistin, D., Regelin, E., Riede, H., Sandu, A., Taraborrelli, D., Tost, H., and Xie, Z.-Q.: The atmospheric chemistry box model CAABA/MECCA-3.0, Geoscientific Model Development, 4, 373–380, https://www.geosci-model-dev.net/4/373/2011/gmd-4-373-2011.pdf, 2011.

Santee, M. L.: Quantifying and confirming our understanding of processes controlling stratospheric ozone: Insights from UARS and Aura MLS, http://www.montreal30.io3c.org/sites/montreal30.io3c.org/files/pictures/19apm/Santee_MPSymp-MLS_Overview.pdf, 2017.

Santee, M. L., Tabazadeh, A., Manney, G. L., Salawitch, R. J., Froidevaux, L., Read, W. G., and Waters, J. W.: UARS Microwave Limb Sounder HNO3 observations: Implications for Antarctic polar stratospheric clouds, Journal of Geophysical Research, 103, 13 285–13 313, 1998.

Santee, M. L., Lambert, A., Read, W. G., Livesey, N. J., Cofield, R. E., Cuddy, D. T., Daffer, W. H., Drouin, B. J., Froidevaux, L., Fuller, R. A., Jarnot, R. F., Knosp, B. W., Manney, G. L., Perun, V. S., Snyder, W. V., Stek, P. C., Thurstans, R. P., Wagner, P. A., Waters, J. W., Muscari, G., de Zafra, R. L., Dibb, J. E., Fahey, D. W., Popp, P. J., Marcy, T. P., Jucks, K. W., Toon, G. C., Stachnik, R. A., Bernath, P. F., Boone, C. D., Walker, K. A., Urban, J., and Murtagh, D.: Validation of the Aura Microwave Limb Sounder HNO3 measurements, Journal of Geophysical Research: Atmospheres, 112, 2007JD008 721, http://onlinelibrary.wiley.com/doi/10.1029/2007JD008721/full, 2007.

Seinfeld, J. H. and Pandis, S. N.: Atmospheric Chemistry and Physics: From Air Pollution to Climate Change, John Wiley & Sons, Incorporated, New York, UNITED STATES, 2016.

Sheese, P. E., Walker, K. A., Boone, C. D., McLinden, C. A., Bernath, P. F., Bourassa, A. E., Burrows, J. P., Degenstein, D. A., Funke, B., Fussen, D., Manney, G. L., McElroy, C. T., Murtagh, D., Randall, C. E., Raspollini, P., Rozanov, A., Russell III, J. M., Suzuki, M., Shiotani,

5   M., Urban, J., Clarmann, T. V., and Zawodny, J. M.: Validation of ACE-FTS version 3.5 NOy species profiles using correlative satellite measurements, Atmospheric Measurement Techniques, 9, 5781–5810, https://www.atmos-meas-tech.net/9/5781/2016/amt-9-5781-2016.pdf, 2016.

Singh, H., Chen, Y., Tabazadeh, A., Fukui, Y., Bey, I., Yantosca, R., Jacob, D., Arnold, F., Wohlfrom, K., Atlas, E., Flocke, F., Blake, D., Blake, N., Heikes, B., Snow, J., Talbot, R., Gregory, G., Sachse, G., Vay, S., and Kondo, Y.: Distribution and fate of selected oxygenated

10   organic species in the troposphere and lower stratosphere over the Atlantic, Journal of Geophysical Research: Atmospheres, 105, 3795–3805, https://agupubs.pericles-prod.literatumonline.com/doi/full/10.1029/1999JD900779, 2000.

Singh, H., Chen, Y., Staudt, A., Jacob, D., Blake, D., Heikes, B., and Snow, J.: Evidence from the Pacific troposphere for large global sources of oxygenated organic compounds, Nature, 410, 1078, https://www.nature.com/articles/35074067.pdf, 2001.

Singh, H. B.: Reactive nitrogen in the troposphere, Environmental science & technology, 21, 320–327, 1987.

15   Spang, R., Remedios, J. J., and Brarkley, M. P.: Colour indices for the detection and differentiation of cloud types in infrared limb emission spectra, Advances in Space Research, 33, 1041–1047, /science/article/pii/S0273117703005854/pdfft?md5= 1e01c4a59e7a98f03118799b17f4e0a1&pid=1-s2.0-S0273117703005854-main.pdf, 2004.

Stiller, G. P., ed.: The Karlsruhe Optimized and Precise Radiative transfer Algorithm (KOPRA), vol. FZKA 6487 of *Wissenschaftliche Berichte*, Forschungszentrum Karlsruhe, 2000.

20   Stohl, A., Forster, C., Frank, A., Seibert, P., and Wotawa, G.: Technical note: The Lagrangian particle dispersion model FLEXPART version 6.2, Atmospheric Chemistry and Physics, 5, 2461–2474, https://www.atmos-chem-phys.net/5/2461/2005/acp-5-2461-2005.pdf, 2005.

Sèze, G., Pelon, J., Derrien, M., Le Gléau, H., and Six, B.: Evaluation against CALIPSO lidar observations of the multi-geostationary cloud cover and type dataset assembled in the framework of the Megha-Tropiques mission, Quarterly Journal of the Royal Meteorological Society, 141, 774–797, https://rmets.onlinelibrary.wiley.com/doi/pdf/10.1002/qj.2392, 2015.

25   Tissier, A.-S. and Legras, B.: Convective sources of trajectories traversing the tropical tropopause layer, Atmospheric Chemistry and Physics, 16, 3383–3398, https://www.atmos-chem-phys.net/16/3383/2016/acp-16-3383-2016.pdf, 2016.

Ungermann, J., Pan, L. L., Kalicinsky, C., Olschewski, F., Knieling, P., Blank, J., Weigel, K., Guggenmoser, T., Stroh, F., Hoffmann, L., and Riese, M.: Filamentary structure in chemical tracer distributions near the subtropical jet following a wave breaking event, Atmospheric Chemistry and Physics, 13, 10 517–10 534, https://www.atmos-chem-phys.net/13/10517/2013/acp-13-10517-2013.pdf, 2013.

30   Ungermann, J., Ern, M., Kaufmann, M., Müller, R., Spang, R., Ploeger, F., Vogel, B., and Riese, M.: Observations of PAN and its confinement in the Asian summer monsoon anticyclone in high spatial resolution, Atmospheric Chemistry and Physics, 16, 8389–8403, http://www.atmos-chem-phys.net/16/8389/2016/acp-16-8389-2016.pdf, 2016.

Vogel, B., Günther, G., Müller, R., Grooß, J.-U., and Riese, M.: Impact of different Asian source regions on the composition of the Asian monsoon anticyclone and of the extratropical lowermost stratosphere, Atmospheric Chemistry and Physics, 15, 13 699–13 716, http:

35   //www.atmos-chem-phys.net/15/13699/2015/acp-15-13699-2015.pdf, 2015.

Vogel, B., Günther, G., Müller, R., Grooß, J.-U., Afchine, A., Bozem, H., Hoor, P., Krämer, M., Müller, S., Riese, M., Rolf, C., Spelten, N., Stiller, G. P., Ungermann, J., and Zahn, A.: Long-range transport pathways of tropospheric source gases originating in Asia into

the northern lower stratosphere during the Asian monsoon season 2012, Atmospheric Chemistry and Physics, 16, 15 301–15 325, https://www.atmos-chem-phys.net/16/15301/2016/acp-16-15301-2016.pdf, 2016.

Vogel, B., Müller, R., Günther, G., Spang, R., Hanumanthu, S., Li, D., Riese, M., and Stiller, G. P.: Lagrangian simulations of the transport of young air masses to the top of the Asian monsoon anticyclone and into the tropical pipe, Atmospheric Chemistry and Physics, 19, 6007–6034, https://www.atmos-chem-phys.net/19/6007/2019/acp-19-6007-2019.pdf, 2019.

von Clarmann, T., Höpfner, M., Kellmann, S., Linden, A., Chauhan, S., Funke, B., Grabowski, U., Glatthor, N., Kiefer, M., Schieferdecker, T., Stiller, G. P., and Versick S.: Retrieval of temperature, H2O, O3, HNO3, CH4, N2O, ClONO2 and ClO from MIPAS reduced resolution nominal mode limb emission measurements, Atmospheric Measurement Techniques, 2009.

Wang, Y., Ma, Y.-F., Eskes, H., Inness, A., Flemming, J., and Brasseur, G. P.: Evaluation of the CAMS global atmospheric trace gas reanalysis 2003–2016 using aircraft campaign observations, Atmospheric Chemistry and Physics Discussions, pp. 1–36, https://www.atmos-chem-phys-discuss.net/acp-2019-821/acp-2019-821.pdf, 2019.

Wiegele, A., Glatthor, N., Höpfner, M., Grabowski, U., Kellmann, S., Linden, A., Stiller, G., and von Clarmann, T.: Global distributions of C_2H_6, C_2H_2, HCN, and PAN retrieved from MIPAS reduced spectral resolution measurements, Atmospheric Measurement Techniques, 5, 723–734, https://www.atmos-meas-tech.net/5/723/2012/amt-5-723-2012.pdf, 2012.

WMO, ed.: Scientific Assessment of Ozone Depletion: 2018, vol. 58 of *Report / World Meteorological Organization, Global Ozone Research and Monitoring Project*, WMO, Geneva, Switzerland, https://www.esrl.noaa.gov/csd/assessments/ozone/2018/report/2018OzoneAssessment.pdf, 2019.

Wohltmann, I. and Rex, M.: The Lagrangian chemistry and transport model ATLAS: Validation of advective transport and mixing, Geoscientific Model Development, 2, 153–173, https://www.geosci-model-dev.net/2/153/2009/gmd-2-153-2009.pdf, 2009.

Wohltmann, I., Lehmann, R., Gottwald, G. A., Peters, K., Protat, A., Louf, V., Williams, C., Feng, W., and Rex, M.: A Lagrangian convective transport scheme including a simulation of the time air parcels spend in updrafts, Geoscientific Model Development Discussions, pp. 1–26, https://www.geosci-model-dev-discuss.net/gmd-2019-5/gmd-2019-5.pdf, 2019.

Woiwode, W., Oelhaf, H., Gulde, T., Piesch, C., Maucher, G., Ebersoldt, A., Keim, C., Höpfner, M., Khaykin, S., Ravegnani, F., Ulanovsky, A. E., Volk, C. M., Hösen, E., Dörnbrack, A., Ungermann, J., Kalicinsky, C., and Orphal, J.: MIPAS-STR measurements in the Arctic UTLS in winter/spring 2010: Instrument characterization, retrieval and validation, Atmospheric Measurement Techniques, 5, 1205–1228, 2012.

Wolff, M. A., Kerzenmacher, T., Strong, K., Walker, K. A., Toohey, M., Dupuy, E., Bernath, P. F., Boone, C. D., Brohede, S., Catoire, V., von Clarmann, T., Coffey, M., Daffer, W. H., Mazière, M. D., Duchatelet, P., Glatthor, N., Griffith, D. W. T., Hannigan, J., Hase, F., Höpfner, M., Huret, N., Jones, N., Jucks, K., Kagawa, A., Kasai, Y., Kramer, I., Küllmann, H., Kuttippurath, J., Mahieu, E., Manney, G., McElroy, C. T., McLinden, C., Mébarki, Y., Mikuteit, S., Murtagh, D., Piccolo, C., Raspollini, P., Ridolfi, M., Ruhnke, R., Santee, M., Senten, C., Smale, D., Tétard, C., Urban, J., and Wood, S.: Validation of HNO3, ClONO2, and N2O5 from the Atmospheric Chemistry Experiment Fourier Transform Spectrometer (ACE-FTS), Atmospheric Chemistry and Physics, 8, 3529–3562, https://www.atmos-chem-phys.net/8/3529/2008/acp-8-3529-2008.pdf, 2008.

Xiao, Y., Jacob, D. J., and Turquety, S.: Atmospheric acetylene and its relationship with CO as an indicator of air mass age, Journal of Geophysical Research: Atmospheres, 112, https://agupubs.onlinelibrary.wiley.com/doi/full/10.1029/2006JD008268, 2007.

Zahn, A., Weppner, J., Widmann, H., Schlote-Holubek, K., Burger, B., Kühner, T., and Franke, H.: A fast and precise chemiluminescence ozone detector for eddy flux and airborne application, Atmospheric Measurement Techniques, 5, 363–375, https://www.atmos-meas-tech.net/5/363/2012/amt-5-363-2012.pdf, 2012.